

ZnFe₂O₄@WO_{3-x}/Polypyrrole: An Efficient Ternary Photocatalytic System for Energy and Environmental Application

Kundan Kumar Das, Dipti Prava Sahoo, Sriram Mansingh, and Kulamani Parida*

Cite This: *ACS Omega* 2021, 6, 30401–30418

Read Online

ACCESS |



Metrics & More

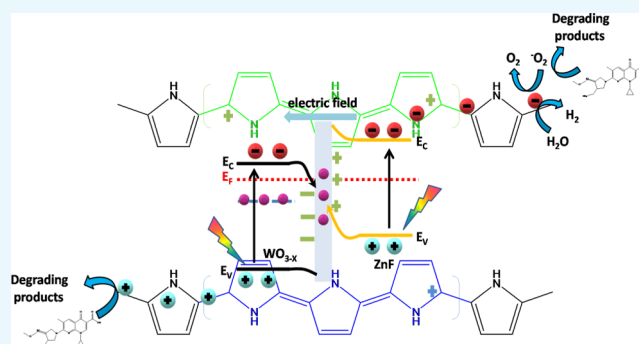


Article Recommendations



Supporting Information

ABSTRACT: Environmental protection and the necessity of green energy have become fundamental concerns for humankind. However, rapid recombination of photoexcitons in semiconductors often gets in the path of photocatalytic reactions and annoyingly suppresses the photocatalytic activity. In this study, a polypyrrole (PPY)-supported step-scheme (S-scheme) ZnFe₂O₄@WO_{3-x} (PZFW15) ternary composite was fabricated by a multistep process: hydrothermal and calcination processes, followed by polymerization. During the formation of the heterojunction, the oxygen vacancy (OV) on WO_{3-x} promotes effective separation and increases the redox power of the photogenerated excitons via the built-in internal electric field of S-scheme pathways between ZnF and WO_{3-x}. The successful construction of the S-scheme heterojunction was substantiated through X-ray photoelectron spectroscopy, experimental calculations, radical trapping experiment, and liquid electron spin resonance (ESR) characterization, whereas the existence of OVs was well confirmed by EPR and Raman analyses. Meanwhile, the PPY served as a supporter, and the polaron and bipolaron species of PPY acted as electron and hole acceptors, respectively, which further enhances the charge-carrier transmission and separation in the ternary PZFW15 photocatalyst. The designed ternary nano hybrid (PZFW15) displays outstanding gemifloxacin detoxification (95%, 60 min) and hydrogen generation (657 μmol h⁻¹), i.e., 1.5 and 2.2 times higher than the normal S-scheme ZFW15 heterostructure and pure ZnFe₂O₄ (ZnF), respectively, with an apparent conversion efficiency of 4.92%. The ESR and trapping experiments indicate that the generated •OH and •O₂⁻ radicals from the PZFW15 photocatalyst are responsible for gemifloxacin degradation. This unique PPY-supported S-scheme heterojunction is also beneficial for the enhanced electron-transfer rate and provides abundant active sites for photocatalytic reactions.



INTRODUCTION

In the last two decades or so, the blue planet has seen vast growth in both human population and industrialization. To satisfy their growing energy needs, a large amount of nonrenewable energy sources, e.g., fossil fuels, is being extensively utilized, which ultimately leads to energy crises and environmental catastrophes. Thus, scientists have worked hard to develop/find a process that is economically viable and environmentally benign.^{1–3} In this direction, the semiconductor-assisted artificial photocatalytic water-splitting reaction toward green fuel hydrogen generation from renewable feedstock (water and sunlight) is the foremost and robust strategy from a sustainability perspective.^{4–6} Numerous photocatalytic materials have been fabricated and experimented with toward the hydrogen evolution reaction to reach the benchmark activity, but unfortunately, the yield is below par for many catalysts and the activity is confined to laboratory-scale production only. Interestingly, n-type spinel ZnFe₂O₄ (ZnF) shows noticeable photocatalytic activities in both the energy and environmental sectors due to its unique

features such as low optical band gap, long-term durability, facile synthesis methods, being cheap, and having an easily tunable morphology.^{7,8} Having said that, faster photoexcited charge-carrier recombination, poor charge diffusion rate, and low charge conductivity are some bottlenecks of ZnF that limit its widespread application.⁹ Therefore, it is hard to find all of the suitable parameters in a single material to achieve the benchmark activity in this field of photocatalytic water reduction reaction.¹⁰ Hence, constructing a promising ZnF-based photocatalytic system with optimum catalytic productivity is highly challenging and needful. To date, a variety of semiconductors with staggered-band structures have been employed to prepare ZnF-based heterojunction catalysts such

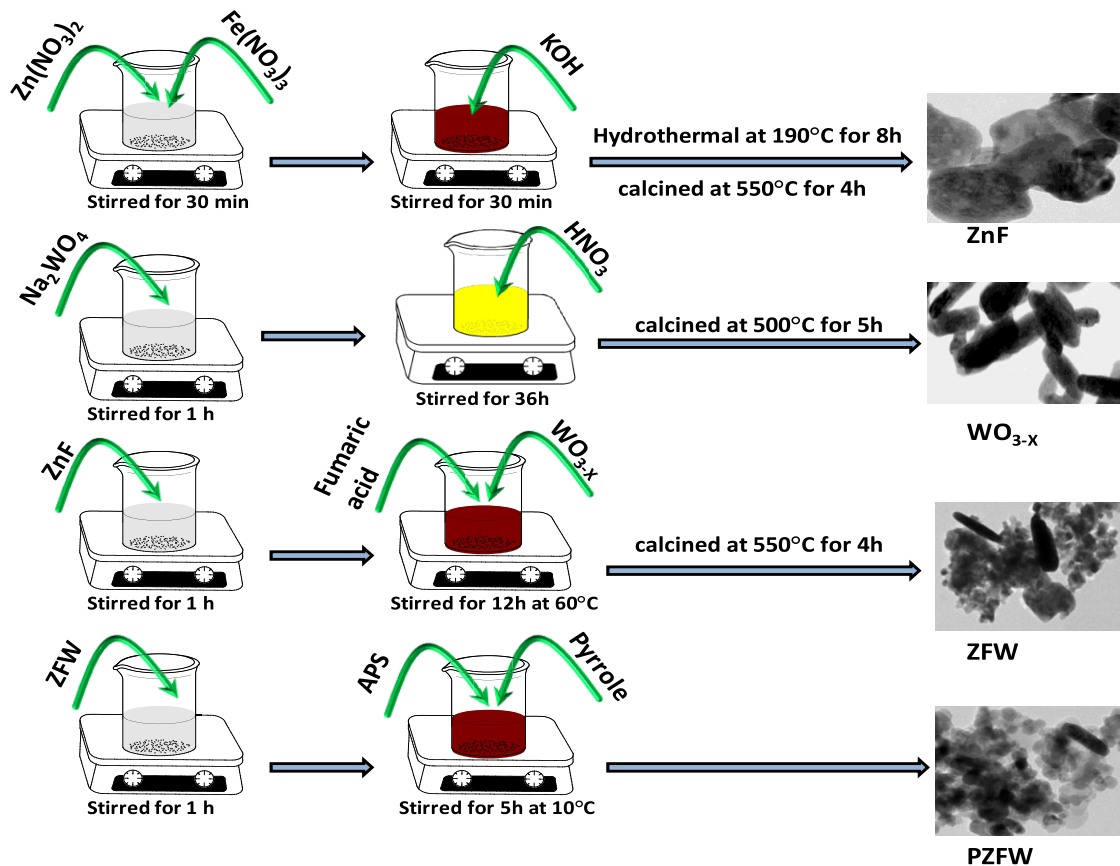
Received: July 13, 2021

Accepted: October 5, 2021

Published: November 1, 2021



Scheme 1. Schematic Representation of the Synthesized PZFW Photocatalyst



as $\text{ZnFe}_2\text{O}_4/\text{g-C}_3\text{N}_4$,¹¹ $\text{ZnFe}_2\text{O}_4/\text{Au}/\text{WO}_3$,¹² $\text{ZnFe}_2\text{O}_4/\text{TiO}_2$,¹³ $\text{SnFe}_2\text{O}_4/\text{ZnFe}_2\text{O}_4$,¹⁴ etc. At the interface of these staggered-heterojunction photocatalysts, the photoproduced e^- migrates from the conduction band (CB) of the higher reduction potential material to the one with a lower potential and simultaneously photoinduced h^+ moves from the higher oxidation valence band (VB) to the lower one via a double charge-transfer pathway. Further, the Coulombic force of attraction does not allow the movement of electron-hole in an opposite/reverse manner.⁶ Although the type-II/staggered junction separates the electron-hole pairs effectively, it has some limitations from kinetic viewpoints. Therefore, the construction of a newly designed S-scheme-based heterojunction has been proposed to address the shortcomings of the conventional type-II junction.^{6,14–16} The step-scheme (S-scheme) heterojunction is a modified version of the Z-scheme orientation, typically composed of two n-type semiconducting materials, i.e., oxidation photocatalyst (OP) and reduction photocatalyst (RP). On interaction, because of the Fermi-level difference, the electron migrates from RP to OP, which further leads to the formation of a built-in electric field at the interface of RP and OP. Further, under illumination, the photoproduced electron at the OP could recombine with the photoinduced hole of the RP owing to the driving force of the built-in electric field.^{15,16} Finally, the useful electron-hole with strong redox capabilities retained at the conduction band of the RP and the valence band of the OP, respectively, leading to effective charge separation. From a macroscopic or microscopic view, the shipment of charge carriers in the S-scheme junction is observed as a “step” or like an “N”, respectively. However, as an innovative conception of heterojunction, S-scheme systems

are still in their infancy. Specifically, in the mediator-free-type heterojunction hybrids, the rates of electron-hole recombination across the junction depend on the formation method and the extent of interfacial contact between the two combining materials.^{16,17} Hence, it is quite challenging to design an efficient semiconductor-semiconductor contact interface in a mediator-free S-scheme-type binary catalytic system. Furthermore, it was observed by different research groups that the presence of surface defects about the junction region alters the electronic and physiochemical features of the binary systems. As is known, oxygen vacancy (OV) is an intrinsic defect found in many metal-oxide-based photocatalytic samples, which plays an important role in the formation of defect-mediated direct S-scheme composites and also facilitates the proper alignment of the energy band due to a strong contact interface between the combining entities.^{17,18} The OVs form an energy-band just below the CB of the defect-induced semiconductor and hence speeds up the electron-hole recombination process operating between the CB of the OV semiconductor and the VB of the other component in the absence of any foreign material (mediator).¹⁹ To date, very few works have fruitfully introduced defect engineering into the step-scheme heterojunction for photocatalysis.²⁰ Therefore, the designing a oxygen vacancy-framed ZnF-WO_{3-x} mediator-free S-scheme-type heterointerface shows a significant increment in catalytic activities compared to its parent material. In the search of a perfect partner for ZnF to construct a propitious vacancy-framed mediator-free S-scheme heterojunction photocatalytic system, oxygen vacancy-induced nonstoichiometric tungsten trioxides (WO_{3-x}) were found to be a better option because of the following benefits: (i) desirable band position, (ii) easy to

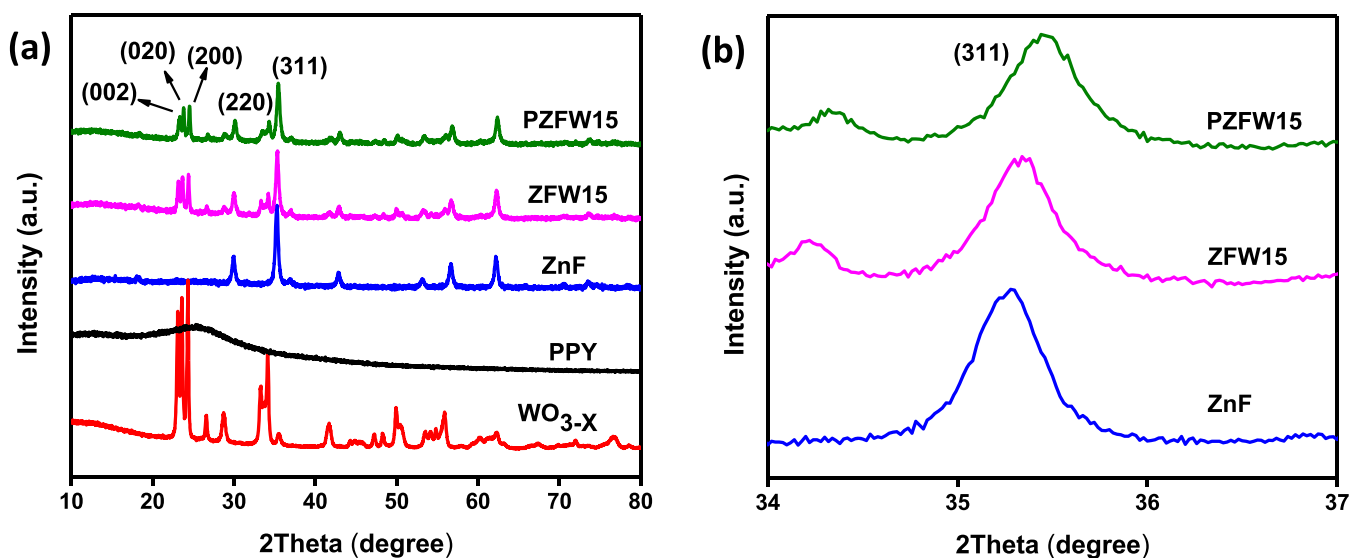


Figure 1. (a) PXRD outlines of PPY, WO_{3-x}, ZnF, ZFW15, and PZFW15 and (b) enlarged PXRD of the (311) diffraction.

prepare, (iii) steady physicochemical parameters, (iv) improved optoelectrical properties, (v) effective exciton separation, etc.^{21–25} However, the observed catalytic performance of the binary hybrid needs further improvement to compare its activity with other reported benchmark photocatalysts. In this respect, a carbonaceous conducting polymer containing π -conjugated frameworks like polyaniline (PANI), polypyrrole (PPY), and polythiophene (PTs) is integrated with various binary composites to uplift their photocatalytic activity. Among the three, PPY has a huge response and widespread applicability because of its high conductivity compared to its other competitors.²⁶ This observed increase in conductivity is due to the formation of defects in the polymer skeleton, leading to the generation of polarons and bipolarons.²⁷ Although the concept of bipolaron-based charge flowing PPY is indecisive yet and lots of debate still on. Moreover, PPY has been largely used for broad-spectrum absorption and efficient charge-carrier separation. Looking at these advantageous properties of PPY, the prepared oxygen-vacancy-mediated ZnF-WO_{3-x} binary heterojunction is integrated with PPY to develop a potential OV-mediated S-scheme-based photocatalytic system.

Herein, we have synthesized a ZnF/WO_{3-x} S-scheme heterojunction with an oxygen vacancy mediator and further supported by polypyrrole through a series of methods, i.e., hydrothermal, calcination, and polymerization. The effectiveness of the S-scheme heterojunction-based ternary photocatalytic was examined toward gemifloxacin (GMF) degradation and H₂ evolution reaction under visible-light irradiation. The detailed GMF degradation pathways were investigated and confirmed by the LCMS and TOC studies. Further, our finding displays that coupling of the S-scheme junction, defect engineering, and radical cations of PPY can enhance the exciton separation, which ultimately improves the H₂ production along with the pollutant degradation capacity of the photocatalyst. This work provides us with a deeper understanding of the development of the high-performance oxygen-vacancy-mediated S-scheme heterojunction photocatalyst for addressing the growing energy and environmental concerns.

Formation Insight of the Ternary Catalytic System (PZFW). The strategy to fabricate polypyrrole-supported ZnFe₂O₄/WO_{3-x} (ZFW) has been shown in Scheme 1. Initially, the hydrothermal and calcination route was adopted for the fabrication of single-domain ZnFe₂O₄ nanoplates/flakes. Further, the nanocapsules of WO_{3-x} were prepared in an acidic medium through the coprecipitation method followed by calcination to produce oxygen-vacancy-oriented WO₃, represented as WO_{3-x} nanocapsules. The thermal treatment leads to the breakage of a few W–O bonds, and as a result, oxygen atoms are removed from the surface, generating oxygen vacancies along with the formation of a W⁵⁺ oxidation state. Further, fumaric acid (organic linker) is used to prepare the binary composite of ZFW, which may have formed a bond between the vacant oxygen site of WO₃ and the Fe 3d orbital of ZnF. Further, the integration of pyrrole with ZFW takes place through the polymerization method, where the σ – π interaction and the strong electrostatic interaction create a strong bonding between the binary hybrid ZFW and PPY, which hold them together firmly, forming the ZnFe₂O₄@WO_{3-x}/polypyrrole (PZFW) ternary composite. All of the above discussions and related chemistry are well justified via different characterization techniques described in the following sections.

RESULTS AND DISCUSSIONS

The crystallinity of the as-synthesized samples was unclogged by X-ray diffraction (XRD) measurements and is presented in Figure 1. Interestingly, all of the characteristic peaks of the prepared ZnF are perfectly indexed to the cubic crystal phase of the spinel ferrite according to JCPDS 01-077-0011, and for pure PPY, a stretched peak is obtained at $2\theta = 25.68^\circ$ corresponding to the (002) plane, which suggests its amorphous nature.^{11,23} Further, the diffraction pattern of WO₃ (Figure S2) was well matched to the standard monoclinic phase according to JCPDS file no. 20-1324.²⁸ Diffraction peaks of the synthesized WO_{3-x} nanoparticles at 23.10, 23.6, and 24.33° are assigned to the (002), (020), and (200) lattice planes of the monoclinic WO₃, respectively. It has been observed that the diffraction peaks of the WO_{3-x} nanoparticle are slightly shifted from the standard patterns, and this shift in

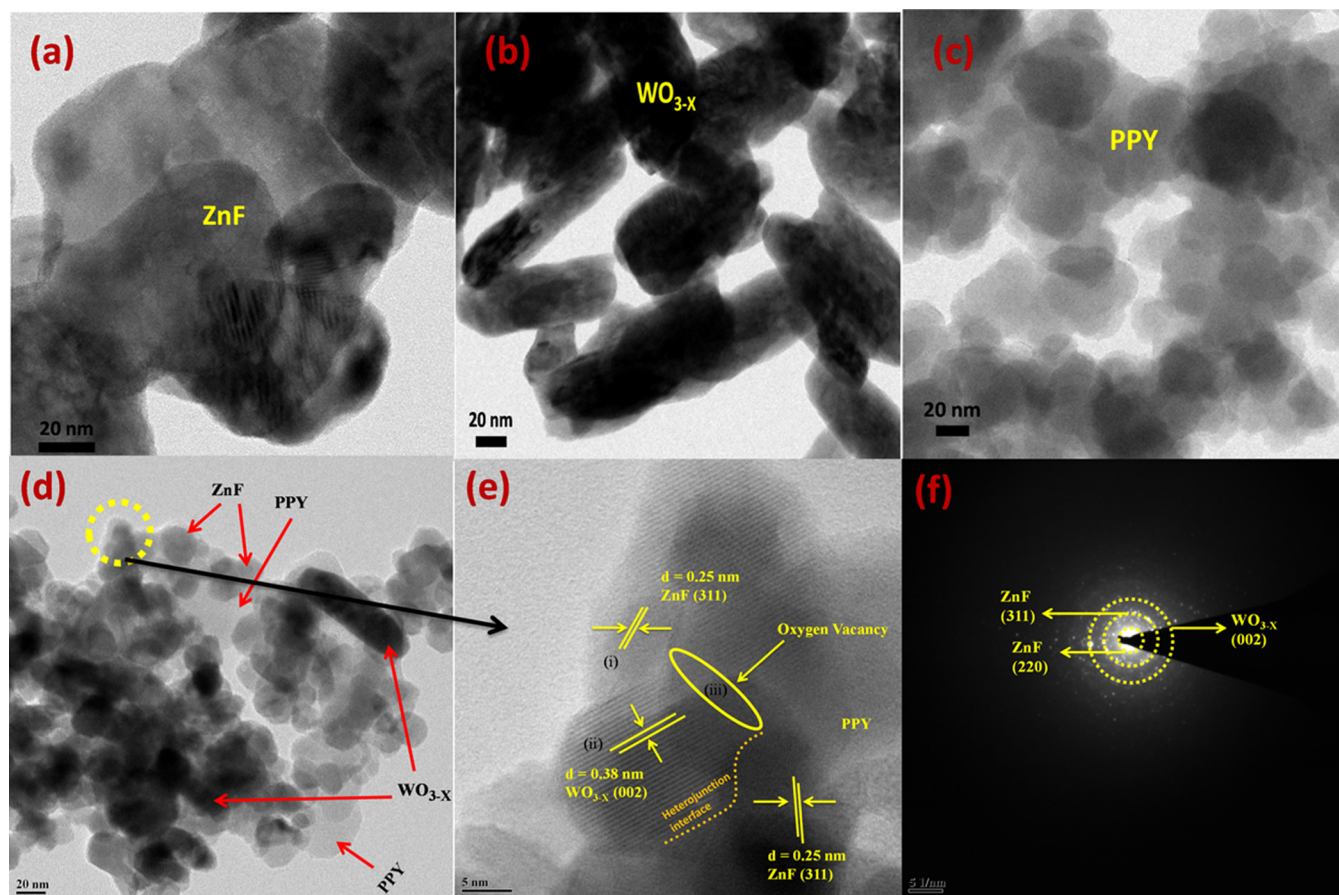


Figure 2. (a–d) TEM images of ZnF, WO_{3-x} , PPY, and PZFW15; (e) HR-TEM and (f) SAED images of the PZFW15 photocatalyst.

the peak positions in the WO_{3-x} suggests the formation of oxygen vacancies in the crystal structure of WO_3 .²⁹ Additionally, the binary composite $\text{ZnFe}_2\text{O}_4@ \text{WO}_{3-x}$ -15% (ZFW15) elucidates the XRD pattern of both the combining specimens, i.e., cubic ZnF and monoclinic WO_{3-x} nanocapsules, indicating the successful materialization of the binary heterostructure. However, after polymerization of the binary hybrid with pyrrol, the formed ternary system $\text{ZnFe}_2\text{O}_4@ \text{WO}_{3-x}$ -15%/polypyrrole (PZFW15) shows a similar XRD sequence to that of ZFW15 with a slight reduction in the peak intensity, which is due to the loading of amorphous PPY. Further, a noticeably higher angle shift of the ZnF(311) plane was visualized in both ZFW15 and PZFW15 composites, respectively, which corroborates the existence of a synergistic interaction between the combining entities in the fabricated heterostructure (Figure 1b). Moreover, no signature peak of PPY was noticed in PZFW15, implying fine dispersal and spreading of the polymeric material in the ternary hybrid. Other than that, no unassigned/unidentified diffraction was obtained, indicating the purity of materials.

The internal and external morphological outlooks of the synthesized samples were characterized by SEM and TEM techniques. The SEM images of WO_{3-x} and PZFW15 are illustrated in Figure S3. The WO_{3-x} sample appears to be capsule-like (Figure S3a), and from the SEM of the PZFW15 ternary heterostructure, it can be observed that ZnF is well attached to the WO_{3-x} along with an aggregated network of PPY (Figure S3b). Further, the color elemental mapping (Figure S3c–h) illustrates the perfect dispersion of Fe, Zn, W, C, O, and N elements in the PZFW15 ternary hybrid.

Additionally, Figure 2 demonstrates the TEM micrographs of neat and ternary composite materials. The nanoplate and nanocapsule-like structures were observed from the TEM images of ZnF and WO_{3-x} samples, respectively, as depicted in Figure 2a,b. Further, the average lengths of ZnF nanoplates and WO_{3-x} nanocapsules were measured to be 36 and 85 nm, respectively. However, PPY seems to be in an agglomerated sphere or sheet form, as observed in Figure 2c. The TEM picture (Figure 2d) of the ternary hybrid gives a clear impression that ZnF, WO_{3-x} , and PPY are closely integrated, which is the main cause of the enhanced activity. Figure 2e displays the HR-TEM image taken from the yellow dotted area (Figure 2d), and the image represents two d-spacing values of 0.25 nm (denoted i) and 0.38 nm (denoted ii) corresponding to (311) and (002) lattice diffractions of ZnF and WO_{3-x} , respectively. The mutilated lattice with a small vacant area (denoted iii) was noticed for WO_{3-x} in the ternary hybrid, suggesting the existence of OV, which remain intact within the lattice after the composite formation.³⁰ For better visibility, a highly enlarged image of Figure 2e has been provided in Figure S4a. Remarkably, a noteworthy interfacial contact was observed between ZnF and WO_{3-x} (Figure 2e), suggesting the formation of the ZFW15 heterostructure. Figure S4b displays the HR-TEM image of PZFW15, where clear lattice fringes of ZnF can be clearly observed. Moreover, no fringes for PPY were observed, suggesting the amorphous nature of the material, which is well consistent with the XRD analysis. Besides, the obtained SAED pattern confirms the polycrystalline nature of the PZFW15 sample, along with the concentric rings representing the (311) plane for ZnF and (220), and

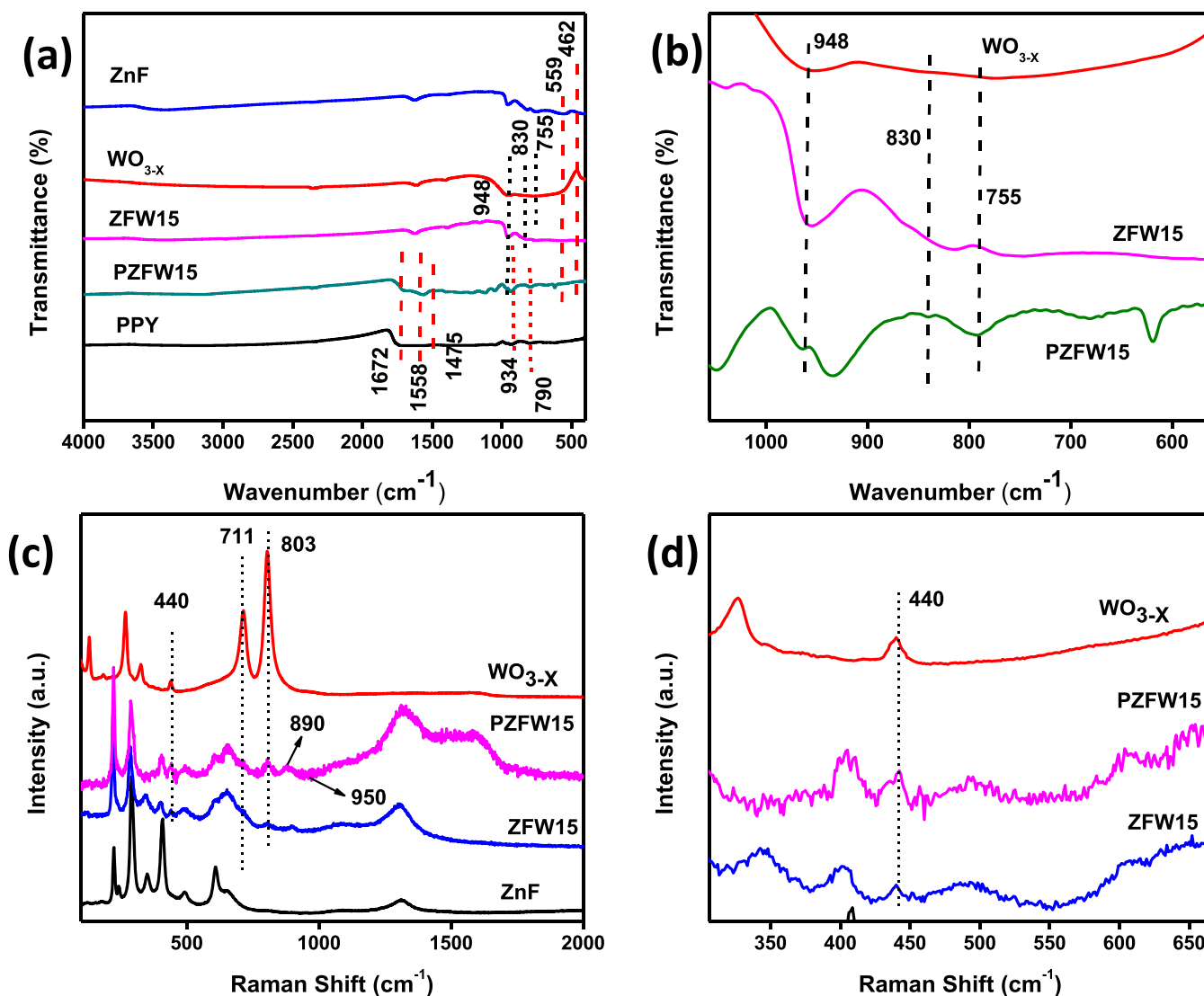


Figure 3. (a) FTIR spectra of ZnF, WO_{3-x}, PPY, ZFW15, and PZFW15; (b) enlarged FTIR image showing insertion of WO_{3-x} in ZFW15 and PZFW15; (c) Raman analyses of ZnF, WO_{3-x}, ZFW15, and PZFW15; and (d) enlarged Raman image of OV's.

(002) crystal planes for WO_{3-x}, respectively (Figure 2f). Similarly, an enlarged picture of the central area of Figure 2f has been provided in Figure S4c. The enlargement and rescaling of images have been done using advanced Image J software. Furthermore, the EDAX measurement (Figure S5) provides a sturdy confirmation regarding the copresence of Fe, Zn, W, C, O, and N elements in PZFW15, revealing the purity of the materials.

Figure 3a depicts the FTIR spectra of as-synthesized materials (ZnF, WO_{3-x}, PPY, ZFW15, and PZFW15) to ascertain the presence of different functional groups and verify the concept of polarons and bipolarons. The vibrational bands located at 462 and 559 cm⁻¹ confirm the existence of metallic groups of ZnF.³¹ As shown in the figure, the evident absorption bands at 755, 830, and 948 cm⁻¹ for WO_{3-x} can be attributed to the bending, asymmetric, and terminal stretching vibrations of the W–O–W moiety, respectively.²¹ The IR bands of the solitary PPY positioned at 790 and 934 cm⁻¹ certify the complete polymerization of pyrrole, which is further confirmed by the appearance of trademark bands at 1475 and 1558 cm⁻¹, respectively.²⁶ Moreover, a characteristic vibrational band is observed at 1672 cm⁻¹, which points out

the formation of free charge carriers, i.e., polaron and bipolaron species. Kumar et al. also reported a similar type of explanation over PPY-modified g-C₃N₄.²⁷ In comparison to the parent materials, the vibrational modes of ZnF and WO_{3-x} with reduced intensity and slight shifting are found in the binary ZFW15 heterostructure, suggesting a close interaction between the two (Figure 3b). Further, the featuring peaks associated with PPY are detected in the PZFW15 hybrid, confirming the successful polymerization of pyrrole on the surface of the ZFW15 heterostructure. For a better comparison, the FTIR spectra of both WO₃ and WO_{3-x} have been provided in Figure S6. Moreover, the existence of functional groups and the generation of polaron and bipolaron could also be established from Raman analysis. Raman polarization signals are intensely sensitive to subtle changes in bond vibrations that may be caused due to phase transition and defects. Figure 3c represents the Raman scattering of solitary ZnF, WO_{3-x}, and PPY along with ZFW15 and PZFW15 hybrid samples sequentially. The Raman signals of ZnF located at 350, 408, 494, and 610 cm⁻¹ can be attributed to the symmetrical vibrations of the cubic spinel ferrite. The highlighted Raman signals above and below 600 cm⁻¹ confirm the presence of

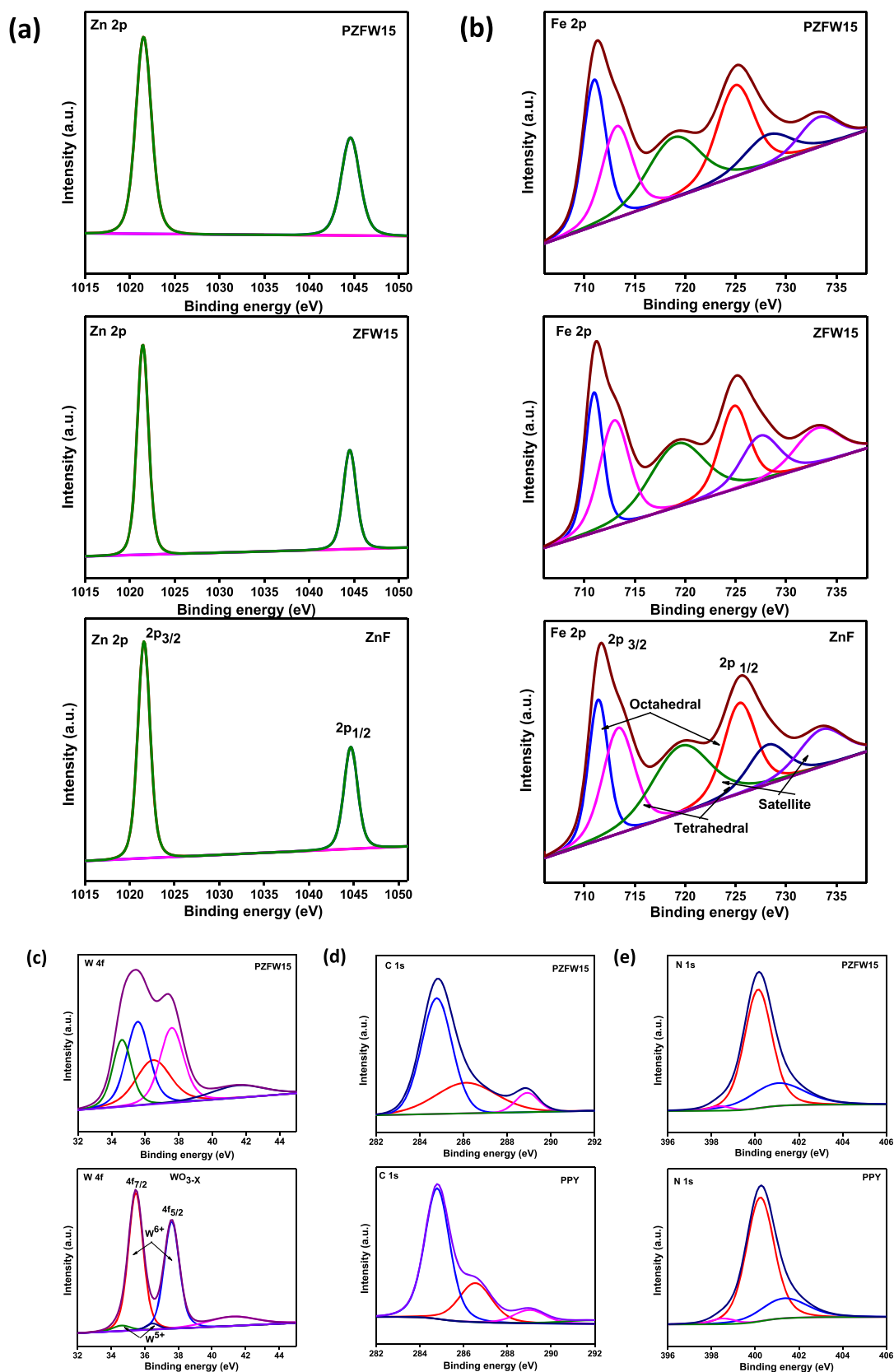


Figure 4. High-resolution deconvoluted XPS spectra of (a) Zn 2p, (b) Fe 2p, (c) W 4f, (d) C 1s, and (e) N 1s of ZnF, WO_{3-x} , PPY, ZFW15, and PZFW15.

tetrahedral (AO_4) and octahedral (BO_6) species.³² Further, the Raman polarization mode of WO_{3-x} shows four active bands at 265, 324, 717, and 811 cm^{-1} in the measured spectral range.

Among them, the bands at 717 and 811 cm^{-1} correspond to stretching and bending modes such as W–O stretching, W–O bending, and O–W–O deformation motion, respectively,

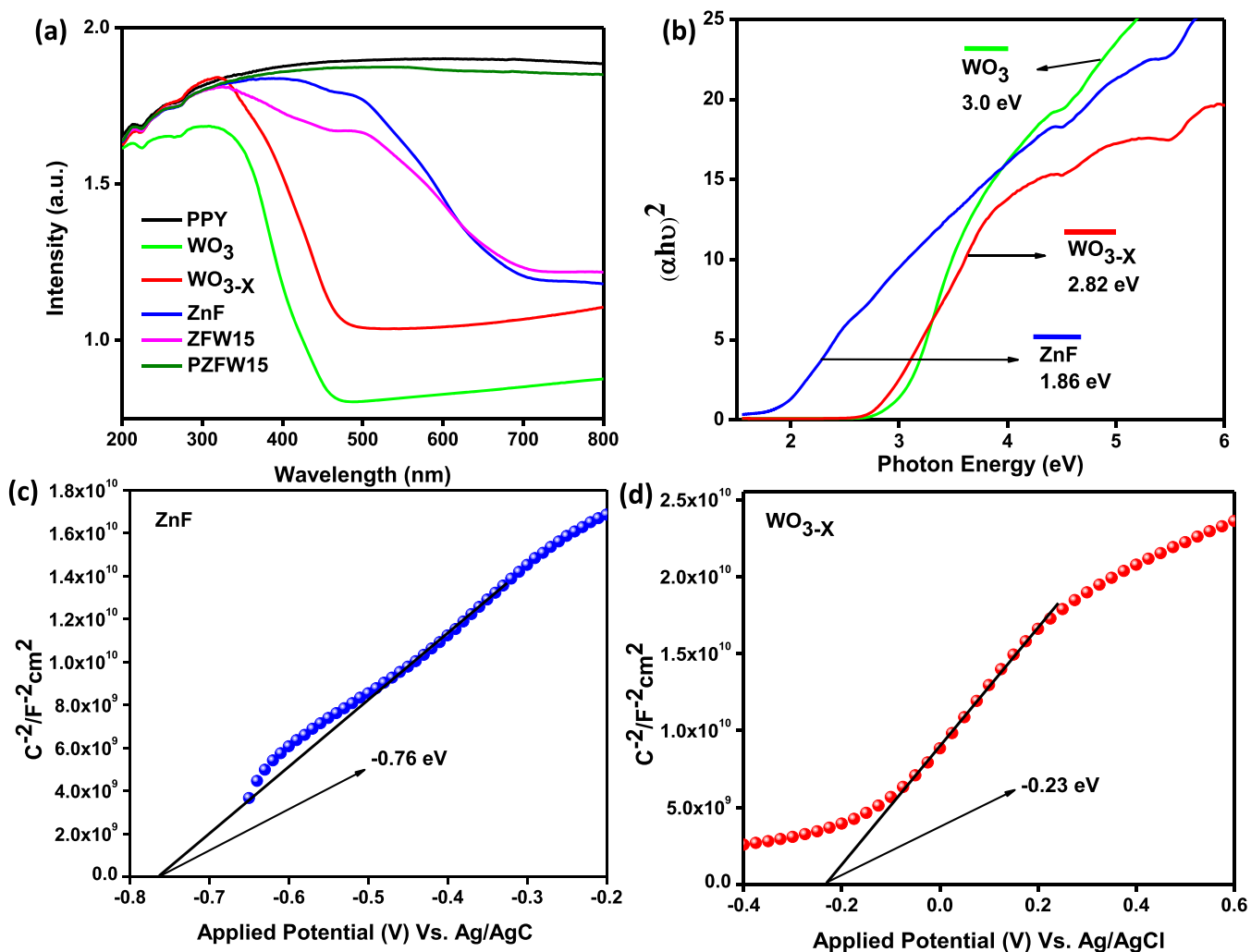


Figure 5. (a) UV-vis absorption spectra; (b) Tau plots of ZnF, WO₃, WO_{3-X}, ZFW15, and PZFW15; M-S plots of (c) ZnF and (d) WO_{3-X}.

while the peaks at a lower frequency explain the bending modes of O–W–O with a bridging oxygen atom.^{33,34} Moreover, similar types of Raman modes were obtained for the WO₃ specimen with a slight shifting in the band position, as provided in Figure S7a. More interestingly, the appearance of an additional band at 440 cm⁻¹ for WO_{3-X} in comparison to neat WO₃ indicates the presence of defective oxygen species, which plays a vital role in the charge separation and transfer mechanism.³⁴ Importantly, thermal treatment can remove the surface-adsorbed water species and may hamper the molecular structure in the form of lattice variation or oxygen defects, resulting in dipole moment variation and polarization, which further result in a Raman shift.²¹ Moreover, from the Raman bands of PPY (Figure S7b), it was observed that the peaks encountered at 890 and 995 cm⁻¹ are ascribed to the bipolaron and polaron vibrations. Han et al. also reported a similar type of vibration.³⁵ The appearance of these two peaks justifies the generation of polarons and bipolarons within the ternary system, which is consistent with IR results. Additionally, two wide Raman humps visualized at 1320 and 1520 cm⁻¹ correspond to the C=C backbone stretching and C–N asymmetrical stretching, respectively.³⁶ Further, the appearance of a Raman peak at 445 cm⁻¹ wavenumber confirms the existence of OVs in the ternary composite (PZFW15). The successful formation/creation of OVs in WO_{3-X}, ZFW15, and

PZFW15 can be well-observed from the magnified Raman image shown in Figure 3d. The characteristic Raman bands of PPY are also detected in the PZFW15 heterostructure, confirming the successful formation of the ternary composite. Henceforth, a conclusion from Raman analysis is drawn that oxygen vacancies along with polarons and bipolarons have been introduced because of lattice deformation and polymerization process, respectively.

XPS measurements were executed to study the surface chemical status and the electronic environment and to gain insights into constituent elements' bonding interaction. The wide survey spectra prominently confirm that the element contains a pure ZnF, ZFW15, and PZFW15 ternary hybrid, i.e., the presence of C, N, O, W, Fe, and Zn (Figure S8), and shows a good correlation with EDX data. The high-resolution XPS spectra of ZnF, ZFW15, and PZFW15 photocatalysts have been depicted in Figure 4. Figure 4a displays the Zn 2p deconvoluted XPS spectra of the ZF sample where peaks situated at 1021.6 and 1044.7 eV convey the existence of 2p_{3/2} and 2p_{1/2} spin states, respectively, with an oxidation state of +2, which further indicates the tetrahedral coordination of Zn in the ZnF material. It can be seen from Figure 4b that the deconvoluted 2p spectra can be classified into two groups of three peaks each arising from the spin–orbit coupling at the 2p_{1/2} (711.4 eV) and 2p_{3/2} (725.5 eV) states. In detail, the

three subpeaks of each group correspond to an octahedral structure, a tetrahedral structure, and a satellite peak, respectively.^{31,37} In comparison to pure ZnF, the Zn 2p and Fe 2p XPS peaks in the binary and ternary heterostructures show a negative drift in the binding energy of about 0.2–0.4 eV, suggesting an increase of the electron density within the composites. Further, Figure 4c displays the fitted W 4f spectrum, where the observed BEs at 35.4 (4f_{7/2}) and 37.5 eV (4f_{5/2}) represent the +6 oxidation state of W in WO_{3-x}, whereas the peaks positioned at 34.7 (4f_{7/2}) and 36.6 eV (4f_{5/2}) in the shoulder region of the spectra suggest the presence of W⁵⁺.^{34,38,39} The occurrence of W⁵⁺ with a small peak area further confirms the occurrence of nonstoichiometric oxygen vacancies in WO_{3-x}.²¹ However, the BE of W 4f (4f_{7/2} and 4f_{5/2} spin states) in the PZFW15 specimen undergoes a higher energy shift, implying the reduction of electron concentration surrounding the tungsten element in the ternary hybrid photocatalyst. The relative concentration of W⁵⁺ to W⁶⁺ was approximately determined using the included area of every peak in the W 4f spectra. The increased concentration of W⁵⁺ in PZFW15 indicates that loading of PPY does not hamper the defects of WO_{3-x}. Figure S9 illustrates the deconvoluted O 1s spectrum of ZnF, ZFW15, and PZFW15 catalysts, respectively. The O 1s plot of ZF bulges out two fitted peaks (O1 and OIII) located at 530.4 and 532.3 eV, respectively, representing the lattice oxygen associated with the metal oxide and surface-adsorbed molecules. There was a slight negative shifting of both XPS peaks (O1 and OIII) in the binary and ternary systems, which explains the change in the electron environment around O 1s and also confirms the construction of the heterostructure. However, an additional peak denoted OII was found in ZFW15 (531.1 eV) and PZFW15 (531.2 eV) systems, which related to the presence of oxygen vacancy.⁴⁰ The binding energy along with the peak intensity of OII in ZFW15 and PZFW15 is high compared to that of WO_{3-x} (Figure S9), referring to the higher amount of oxygen vacancy presence, which is well consistent with the Raman analysis. From the above XPS analysis, we observed a negative or lower binding energy shift for Zn and Fe and a positive or higher BE drift in W of the PZFW15 sample. Besides, Figure 4d represents the deconvoluted C 1s spectra with peaks located at binding energies of 284.8, 286.5, and 288.9 eV, which are ascribed to the sp² C–C bonds or adventitious carbon, polaron (=C–NH^{•+}), and bipolarons (-C=N⁺) bonds of pyrrole rings, respectively. Similarly, the N 1s spectra (Figure 4e) deconvoluted into three peaks observed at BE 398.4, 400.2, and 401.4 eV and represent the sp²-hybridized atoms (C=N–C) as well as stand for quinoid amines (=N⁻), polaron state (-NH^{•+}) followed by -NH of nitrogen in the pyrrole ring.^{26,27} These results completely confirm the presence of polarons and bipolarons in the PPY. In contrast, a negative binding energy shift of C 1s and N 1s spectra was observed for the PZFW15 composite, suggesting the larger electron density around PPY in the ternary heterostructure. The whole XPS results demonstrated that there were S-scheme charge-transfer phenomena occurring in between ZnF and WO_{3-x}, and the electron cloud transferred from both ZnF and WO_{3-x} to the PPY surface and carried the photocatalytic reduction/oxidation reaction, respectively.⁴¹ In addition to XPS, the formation of OV_s and the generation of radical cations were perceived from EPR measurements. Figure S10 illustrates the EPR signals of WO_{3-x}, ZFW15, and PZFW15 samples. All of these samples exhibit a strong paramagnetic signal at a g-value of 1.97,

corresponding to the existence of unpaired electrons trapped in oxygen vacancy. In comparison to WO_{3-x}, an intense paramagnetic signal was found for ZFW15, which describes the increased amount of oxygen vacancies. More importantly, an enhancement in the EPR signal was encountered after polymerization, and this enhancement of the signal signifies the generation of free radicals during the synthesis of PPY, which further verifies the generation of polaron and bipolaron species.²⁷

The photophysical properties of the designed samples were determined using a UV–vis diffuse reflectance study, plotted in Figure 5a. Generally, the spinel ZnF exhibits strong absorption edge close to 700 nm, which is due to the shipment of photoexcitons from the valence band to the conduction band. The WO₃ shows a strong absorption in the UV region with an absorption edge at 470 nm. However, the WO_{3-x} specimen exhibits a significant bathochromic/red shift of the absorption edge from 470 to 490 nm due to oxygen vacancies resulting from the thermal treatment. It is well known that OV_s create a defect energy level below the conduction band of WO₃. Hence, the enhancement in light absorption and the shifting of the absorption edge toward the visible region suggest that the electron transition occurs between the valence bands and the energy level of oxygen vacancies, which have been created due to partial reduction of WO₃ and formation of nonstoichiometric WO_{3-x}.²² On the contrary, PPY displays absorption spectra covering the entire visible to near-IR region, owing to the black nature of the samples. The optical absorption of PPY in the visible region is attributed to the π – π^* transition in benzenoid and quinoid units. In comparison to WO_{3-x}, a red shift in the photon absorption can be observed for the ZFW15 composite. Further, the ternary catalytic system (PZFW15 hybrid) ominously shows wide light-capturing, resulting in a large amount of photoproduced e⁻–h⁺ pairs and higher photocatalytic activities. The energy-gap values for WO₃, WO_{3-x}, and ZnF samples were determined to be 3.0, 2.8, and 1.86 eV, respectively, from the Tau plot using the Kubelka formula, as shown in Figure 5b. The energy band of OV_s is estimated to be 0.7 eV below the conduction band (CB) of WO₃, which has been derived from the maximum absorption of 535 nm in the tailed region of WO_{3-x}.

Thereafter, Mott–Schottky analyses (MS) were performed to gather more information regarding the nature of the semiconducting material, charge migration in the liquid/electrolyte solution, donor density, and band-edge potential (CB or VB), as it is a quite crucial parameter for depicting the reaction mechanism. A positive slope for both ZnF and WO_{3-x} samples confirms the n-type nature of both the photocatalysts with flat band potentials of –0.76 and –0.23 eV vs Ag/AgCl, respectively (Figure 5c,d). Furthermore, the charge-carrier density (N_d) was obtained from the M–S plot, based on eq 1.⁴²

$$N_d = (2/\epsilon\epsilon_0e)[d/(1/C^2)/dV]^{-1} \quad (1)$$

where C represents the capacitance, ϵ is the dielectric constant, ϵ_0 is the permittivity of a vacuum, e is the elementary charge value, and N_d is the donor density. Consequently, the donor density of PZFW15 was found to be $8.5 \times 10^{17} \text{ cm}^{-3}$, which is greater than that of the corresponding ZnF ($5.1 \times 10^{16} \text{ cm}^{-3}$) and ZFW15 ($4.8 \times 10^{17} \text{ cm}^{-3}$) semiconductors. The observed high N_d of the ternary hybrid is associated with effective charge separation and migration, which can be attributed to the positive effect of free charge on the binary heterojunction

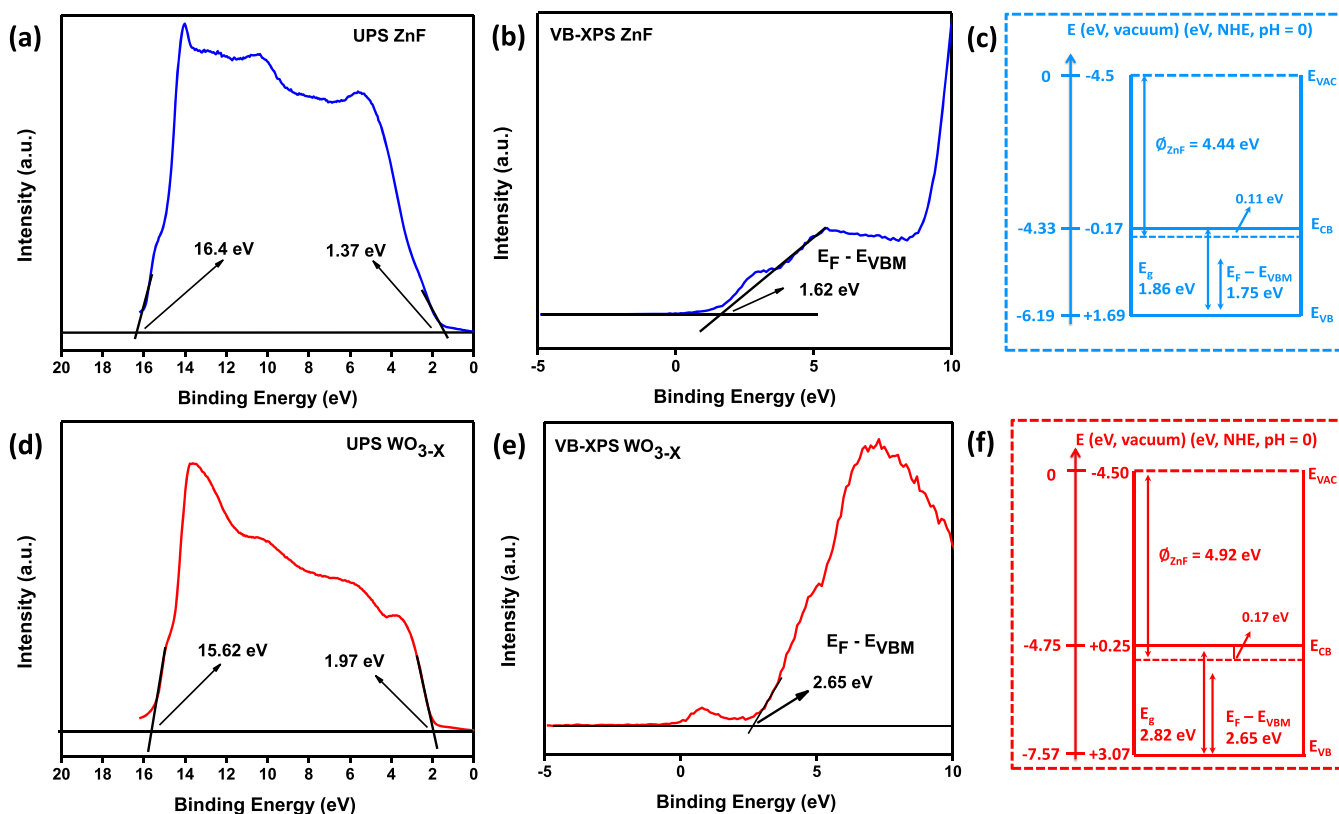


Figure 6. (a, d) UPS spectra of ZnF and WO_{3-x} ; (b, e) VB-XPS spectra ZnF and WO_{3-x} ; and (c, f) energy diagrams of ZnF and WO_{3-x} (vs vacuum and NHE, respectively).

photocatalyst (ZFW15). Further, an increase in donor density leads to the formation of a space-charge layer and builds an electrical field close to the electrode–electrolyte interface. As a consequence, there is improved charge isolation and shipment, thereby boosting the photocatalytic activities.⁴² To further support this conclusion, the Debye lengths (L_D) of ZnF, ZFW15, and PZFW15 were evaluated according to eq 2

$$L_D = (\epsilon_0 \epsilon_r k_B T / 2e^2 N_d)^{1/2} \quad (2)$$

Generally, a smaller value of L_D indicates less transit time and a higher concentration of charge carriers, ultimately leading to better exciton separation. Further, the L_D value of PZFW15 is determined to be nm, which is much smaller than that of the other samples, i.e., ZnF (nm) and ZFW15 (nm), suggesting an enhanced separation efficiency of photoinduced charge carriers, leading to a significant improvement in photocatalytic performance.

Charge-Transfer Mode. The band-edge position of the materials is found to have a direct impact on its redox ability, which happens at the catalyst surface. The estimated band-gap energies for ZnF and WO_{3-x} were 1.86 and 2.82 eV, respectively. The valence band energies (E_v) of ZnF and WO_{3-x} were obtained using ultraviolet photoelectron spectroscopy (UPS). The E_v values for ZnF and WO_{3-x} were calculated to be 6.19 and 7.57 eV. Conduction band (CB) energy (E_c) values of 4.33 (ZnF) and 4.57 eV (WO_{3-x}) were elucidated from the difference between E_g and E_v . For further analysis of band-gap structures of ZnF and WO_{3-x} , XPS-VB measurements were performed to determine their electronic structures. The D -value between the Fermi level (E_F) and the valence band maximum (E_{VBM}) of the as-synthesized ZnF and

WO_{3-x} can be estimated from the VB-XPS spectrum as displayed, and the values were 1.62 and 2.65 eV for ZnF and WO_{3-x} , respectively. Combining the results of the band gap, UPS, and XPS-VB, the work functions (Φ) of ZnF and WO_{3-x} can be calculated as -4.44 and -4.92 eV, respectively.⁴³ The Fermi level of ZnF is found to be exactly at 0.11 eV below the CB, while for WO_{3-x} , the Fermi level lies at 0.17 eV below the CB. As found from the UV–vis analysis, the OV energy state is situated at 0.7 eV lower than the actual CB position, so the OV energy band (vs the vacuum level) will be at -5.45 eV. Gathering the above-calculated data, the energy-level diagrams of ZnF and WO_{3-x} along with UPS and VB-XPS spectra are shown in Figure 6. Additionally, the detailed calculated values related to band-edge positions of ZnF and WO_{3-x} (vs NHE) are supplied in Table S1. More importantly, these calculated energy-level values will help in predicting the electron–hole separation and migration mechanism.

It is believed that the formation of the S-scheme heterojunction through OVs in between ZnF and WO_{3-x} plays a key role in reducing the recombination effect of photoproduced charge carriers, which was further enhanced by the addition of PPY. Henceforth, to provide more convincing evidence in support of the above statement, PL, TRPL, electrochemical impedance spectroscopy (EIS), and transient photocurrent were performed.

The effectual separation of photoexcited charge carriers was again strongly supported by photoluminescence (PL) spectra, as it is a useful technique to explore the transfer and recombination properties of photoexcited charge carriers. Moreover, steady-state PL analysis was used to specify the effect of OVs and free charge carriers of PPY on the lifetime of photoproduced excitons. Figure 7a represents the PL spectra of

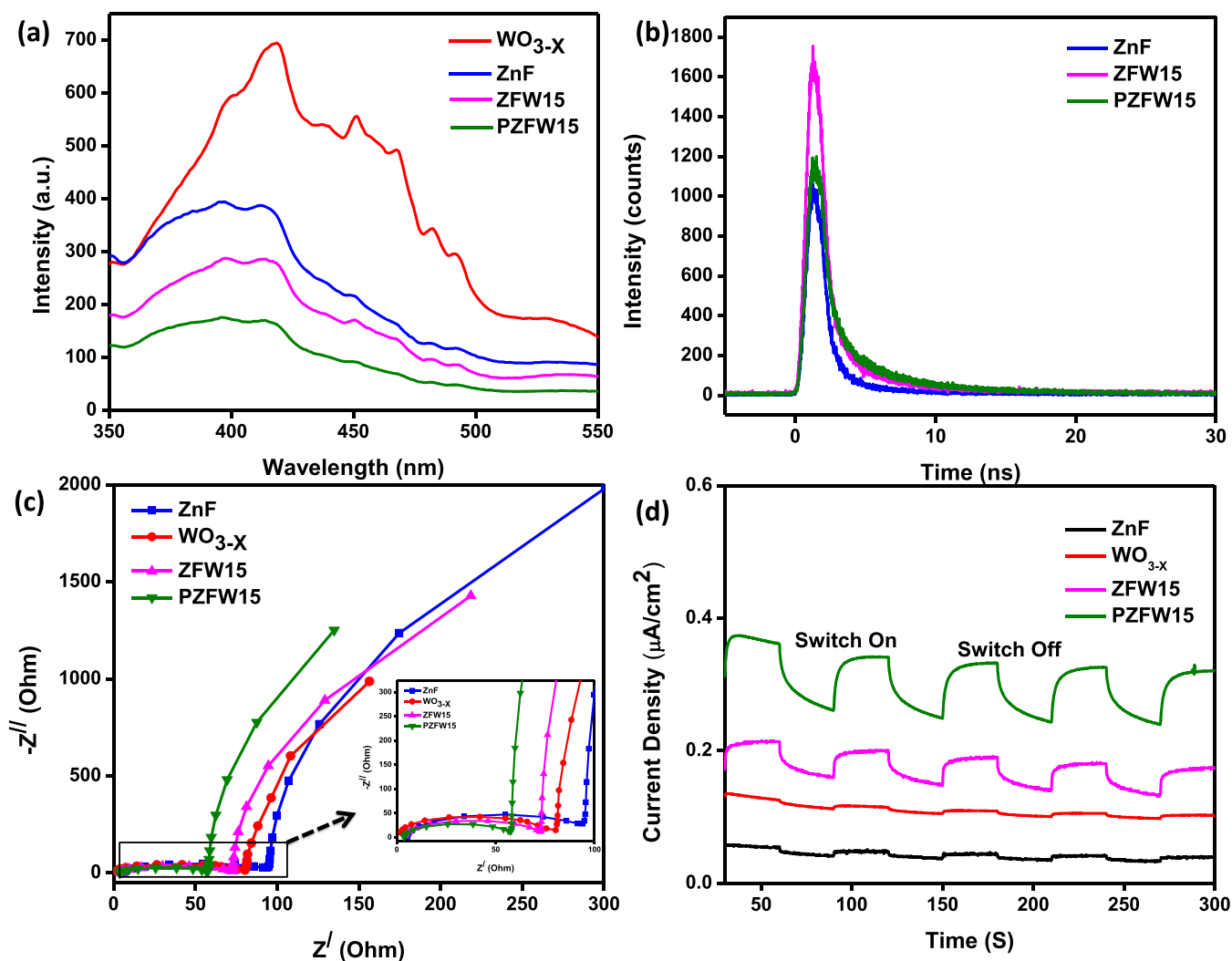


Figure 7. (a) PL, (b) TRPL, (c) EIS (inset: image of the EIS semicircular arc), and (d) TPC of ZnF, WO_{3-x} , ZFW15, and PZFW1 photocatalysts.

ZnF, WO_{3-x} , ZFW15, and PZFW15 at an excitation of 350 nm. In the WO_{3-x} PL spectrum, the intense shoulder peak (420 nm) is attributed to the indirect band-to-band transition and the introduction of surface OV-induced charge-carrier trapping states.²¹ It is easy to find that the luminescence spectrum of parent WO_{3-x} and ZnF displays the strongest magnitude among binary and ternary hybrids, which is induced by the fast recombination of photoproduced charge carriers. However, a reduction in fluorescence intensity is observed for ZFW15, which suggests that the incorporation of WO_{3-x} had efficiently restricted the charge recombination process due to the existence of an oxygen vacancy layer at the interface. The OVs present in WO_{3-x} also play an important role in overpowering the recombination of charge carriers as the electrons in the OV energy band recombine with the holes of HOMO of ZnF, further separating the photoinduced electron–hole pairs. Moreover, an extremely low magnitude of fluorescence intensity (or quenching) was encountered after the introduction of PPY. The oxidative species (polaron and bipolaron) of PPY further traps the charge carriers and increases the lifetime of photoproduced excitons, leading to an increased photoactivity.

Furthermore, time-resolved photoluminescence (TRPL) decay was conducted for gaining in-depth information

regarding the charge-carrier lifetime/recombination and reflects the transfer efficiency of the photogenerated charge carriers. Similarly, the TRPL measurement was also used to explore the effect of OVs and conjugated π -skeleton of PPY on the lifetime of photoproduced charge carriers. As demonstrated in Figure 7b, the spectra were modulated by a biexponential fitting curve consisting of shorter and longer lifetime components. As listed in Table S2, the mean lifetime of ZFW15 was 2.4 ns, which was higher than that of ZnF (1.8 ns) incontrovertibly. The enhanced lifetime of charge carriers in ZFW15 could be ascribed to the formation of an S-scheme-type charge-transfer mechanism between ZnF and WO_{3-x} , where OVs act as charge arbitrators. Specifically, the OVs play the role of arbitrators in establishing a charge-transfer bridge between WO_{3-x} and ZnF, which quickens the transmission and separation of photoproduced charge carriers at the interface of the S-scheme junction.^{17,44}

Further, electrochemical impedance spectroscopy was carried out to investigate the interfacial faradic kinetics along with charge separation. Generally, the arc/diameter of the semicircle in the Nyquist plot informs about the charge-transfer process, and this corroborates with the charge-transfer resistance in the electrolyte solution. Figure 7c highlights the Nyquist plot of synthesized samples. As illustrated, the arc

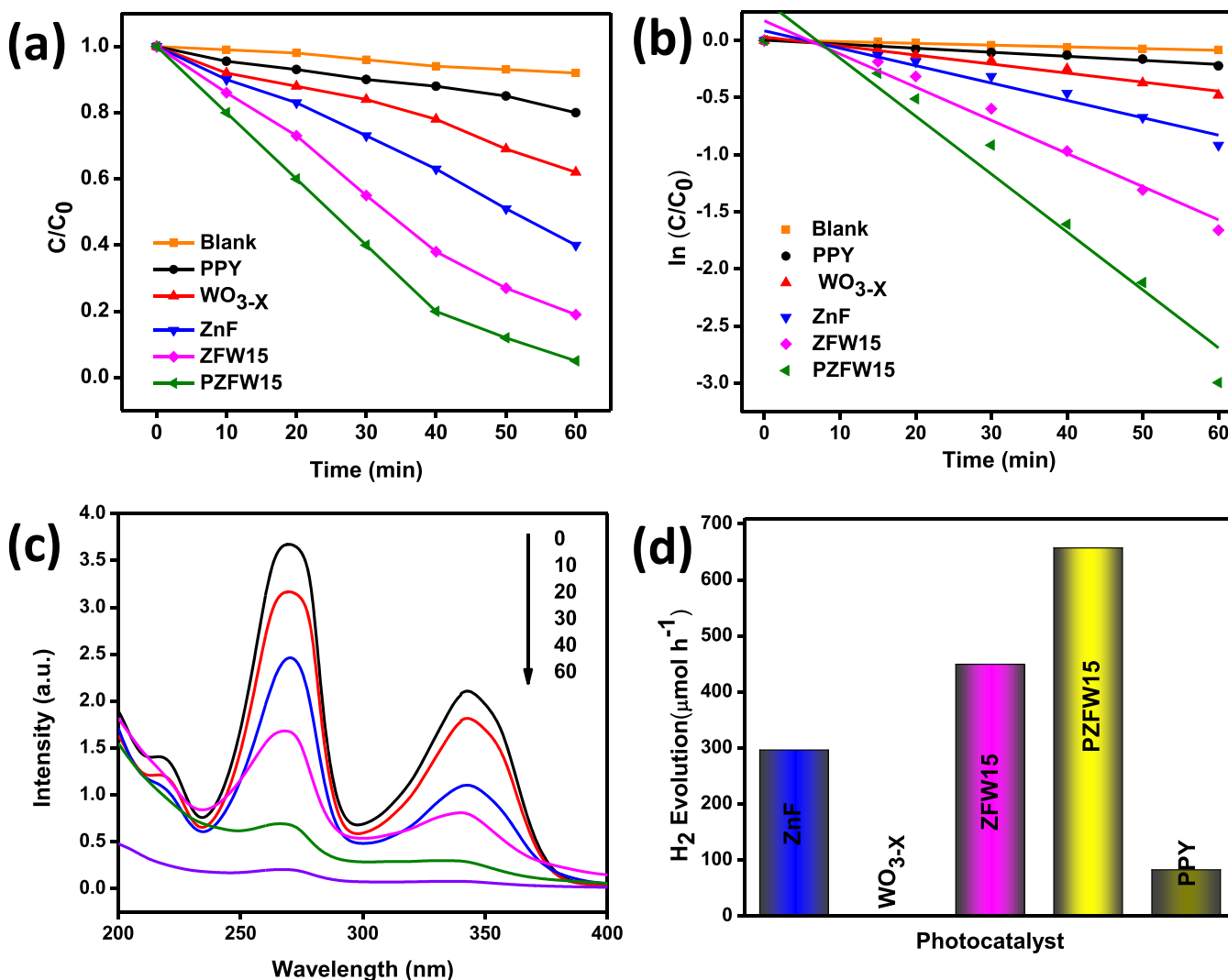


Figure 8. (a, b) Photodegradation of GMF and pseudo-first-order kinetics over all materials. (c) Spectral change of GMF concentration with time. (d) H₂ generation by various photocatalysts.

radius of ZFW15 was smaller than that of the parent materials, signifying a better charge transfer and a reduced charge resistance. This result suggests that the formation of an S-scheme junction through OVs can reduce the resistance and promote productive interfacial-charge migration. The coexistence of W⁵⁺ and W⁶⁺ ions and the intervalence charge transfer between these ions increase the conductivity and decrease the charge-transfer resistance.⁴⁵ Moreover, after polymerization, the PZFW15 ternary hybrid shows an extremely trifling semicircular arc, suggesting that low charge-transfer resistance and high conductance are taking place between the interface of PZFW15 and the electrolyte, which is attributed to the presence of polaron and bipolaron species. For a better comparison, the magnified image of the EIS semicircle at a higher frequency has been shown in the inset in Figure 7c. Thus, more active photogenerated electrons can be easily captured by protons to generate H₂ gas.

To further probe the effects of OVs, polaron, and bipolaron species, the $I-t$ curves were recorded at a bias of 0.2 V during irradiation and dark cycles (Figure 7d). Upon irradiation, the ZFW15 heterostructure shows a rise in the photocurrent followed by a transient decay. This may be caused by the formation of intrinsic defects (OVs) on the surface of WO₃,

which acts as an electron mediator to construct a junction between WO_{3-X} and ZnF.⁴⁴ The existence of oxygen vacancies might change the flow direction of excitons, leading to a stronger redox potential for ZFW15, which is in accord with the electron migration path of the S-scheme photocatalytic system. However, a slightly higher photocurrent was noticed for the PZFW15 sample in comparison to other samples, which may be due to the synergistic impact of both OV-mediated S-schemes along with the presence of polaron and bipolaron populations. Further, effective electron-hole separation and the presence of free charge carriers in the polaron and bipolaron are also responsible for the higher photocurrent. The photoelectrons from the CB of ZnF were trapped by positively charged polaron species of PPY, which were further captured by protons, resulting in H₂ production, whereas holes were captured by bipolaron species and were utilized by the sacrificial agent and the GMF pollutant. The effective photocurrent value of PZFW15 implies more generation, separation, and transfer of excitons.

The photocurrent profiles vs the potential of PZFW15 ternary hybrids along with other prepared photocatalysts showed that the specimens are quite subtle to light illumination and most of the photoproduced electrons travel

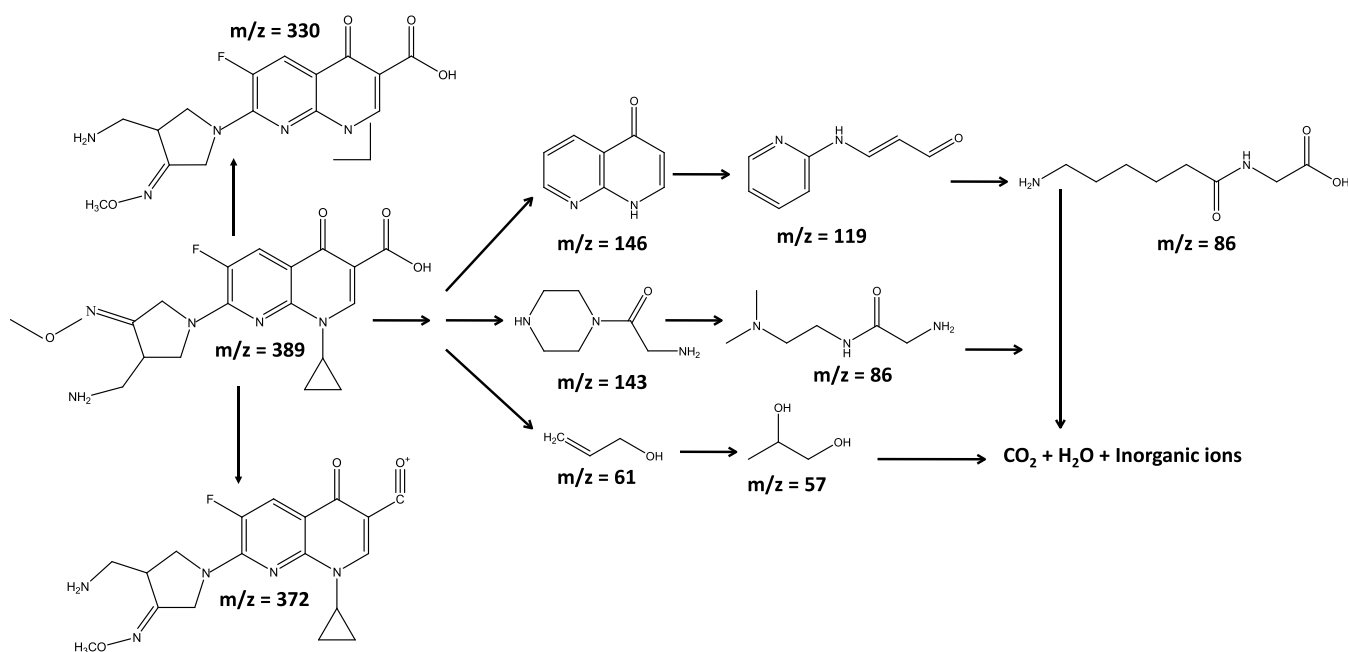


Figure 9. Proposed degradation pathway of GMF over PZFW15.

swiftly across the semiconductor interface. The solitary ZnF and WO_{3-x} display inherent anodic polarization curves, further validating the n-type electronic behavior of counterparts, which is consistent with MS studies. Figure S11 shows the polarization curve of all synthesized photocatalysts under light irradiation at a potential bias of 1.3 V. Outstanding increments in current densities were noticed for the ZFW15 (0.352 mA/cm^2) specimen, which were 2.8- and 32.2-fold higher than that of the pure ZnF and WO_{3-x} materials, respectively. The enhancement of photocurrent can be ascribed to the formation of the S-scheme between WO_{3-x} and ZnF via the oxygen vacancy state. The existence of a defect energy level in the form of oxygen vacancy in WO_{3-x} results in the inter-band-gap state just below the CB, which increases the lifetime of the photoelectrons by trapping them. Moreover, the intervalence charge transfers between W^{5+} and W^{6+} ions are also responsible for the high photocurrent density and conductivity.^{22,45} Interestingly, a further enrichment in current densities was observed after the addition of PPY to ZFW15. The PZFW15 sample displays a maximum current density of 0.624 mA/cm^2 . The polaron and bipolaron species of PPY rapidly attract photogenerated charge carriers, thereby increasing the separation process of electron–hole pairs. It is well-accepted that the higher the magnitude of the photocurrent density response, the greater is the separation and transfer efficiency of photogenerated charge carriers, which ultimately leads to the high photocatalytic activity.

Photocatalytic Activity. Gemifloxacin (GMF) as the fluoroquinolone (FQ) was used to treat bacterial infections by killing the bacteria or hindering their growth. According to the report of the World Health Organization (WHO) published in 2014, continuous and excessive usage of GMF antibiotics leads to serious health and environmental problems such as genotoxicity and antibiotic resistance of bacteria.^{46,47} Before exposure to sunlight, the mixture of catalyst and pollutant was stirred in dark conditions to establish an adsorption–desorption equilibrium. However, minimum adsorption results were obtained, as depicted in Figure S12. The solar-light-

driven GMF degradation was carried out for evaluating the photocatalytic abilities of the as-synthesized samples (Figure 8). Figure 8a displays the GMF detoxification ratio with respect to time over different photocatalysts. Blank experiments were conducted, where GMF was fairly stubborn, suggesting that direct photolysis of the antibiotic could be ignored. The degradation efficiency of GMF for solitary PPY, WO_{3-x} , and ZnF displays a moderate photocatalytic activity corresponding to removal efficiencies of 21, 32, and 60%, respectively. However, the ZFW15 specimen exhibits a handsome photocatalytic degradation activity of 79%, which could be attributed to the efficient charge separation between ZnF and WO_{3-x} . The introduction of OVs in WO_{3-x} acts as a charge mediator to formulate the S-scheme heterojunction between ZnF and WO_{3-x} of the binary system, which efficiently transports and expands the lifespan of photogenerated charge carriers along photon absorptivity. The intervalence charge transfer between the W^{5+} and W^{6+} ions was also responsible for the enhanced photoactivity.^{44,45} Encouragingly, the PZFW15 exhibits an optimal performance with 95% GMF degradation in 60 min of irradiation, which is higher than the others. We attribute this superior activity to the combined effect of the OV-induced S-scheme orientation and polaron and bipolaron species of PPY. Moreover, here we have used PPY as the electron and hole channeling medium in the proposed S-scheme mechanism, where the photogenerated e^- – h^+ pairs were readily available for pollutant degradation. Figure 8b displays that the amplified photocatalytic behavior over different photocatalytic materials was well-observed to follow a pseudo-first-order kinetic model and contended via employing eq 3.

$$\ln\left(\frac{C_0}{C}\right) = k_{\text{app}}t_{1/2} \quad (3)$$

Moreover, by utilizing the above equation, the $t_{1/2}$ was calculated. Generally, $t_{1/2}$ is the amount of time required to degrade GMF into half of its original concentration and can be represented as in eq 4

$$t_{1/2} = 0.693/k_{\text{app}} \quad (4)$$

The rate constant (k_{app}), correlation coefficient factor (R^2), and half-life value ($t_{1/2}$) of GMF degradation have been summarized in Table S3. The PZFW15 specimen displays the highest rate constant with the lowest half-life, which is more than the PPY, ZnF, WO_{3-x} , and ZFW15 photocatalysts. Nevertheless, the ternary heterostructure exhibits an elevated detoxification rate, which is found to be higher than that of the fabricated bare and binary S-scheme heterostructure. The quantitative measurements are well-attested by the drastic decline in absorption intensity of the respective characteristic peak signals near 270 and 343 nm (Figure 8c). Furthermore, the effects of different parameters (catalyst dosage, GMF concentration, cations, and anions) were optimized for the best photocatalyst, and the details have been discussed in the Supporting Information (Figure S13). Further, to identify the intermediate species generated during the photocatalytic degradation of GMF over the PZFW15 ternary heterostructure, LCMS analysis was carried out. The mass spectra of the intermediate during the reaction time (0–60 min) are depicted in Figure S14. A concentrated peak of $m/z = 389$ corresponds to the neat GMF concentration (Figure S14a). After 60 min of reaction, the strength of the peak decreases, as depicted in Figure S14b. The details of the main intermediate products produced from the GMF degradation and the proposed degradation pathway are shown in Figure 9. According to the detected compounds corresponding to their m/z values, three different pathways were proposed as described below. First, the GMF is deprotonated, to generate the fragmentation molecular ion at $m/z = 389$. It must be pointed out that there might be other compounds that resulted ($m/z = 372, 330, \text{ and } 246$) from the GMF dissociation before the formation of smaller fragments, which is narrated in brief as follows. (i) In degradation pathway I, the GMF dissociates into 1,8-naphthyridin-4-one having $m/z = 146$. After that, the oxidation reaction might have occurred and subsequently generated the first ring cleavage products (i.e., 3-(pyridin-2-ylamino) prop-2-enal, $m/z = 119$). The attack of reactive species leads to the cleavage of the pyridine ring of 3-(pyridin-2-ylamino) prop-2-enal to produce *N*-(6-aminohexanoyl) glycine ($m/z = 86$). (ii) In degradation pathway II, the GMF was converted into 2-amino-1-piperazin-1-ylethanone with $m/z = 143$. Then, *N*-[2-(dimethylamino) ethyl] glycinamid ($m/z = 86$) was formed through ring-opening of 2-amino-1-piperazin-1-ylethanone. (iii) In pathway III, the DMF cleaved into 2-propen-1-ol ($m/z = 61$) on the PZFW15 nanocomposite, and then, further oxidation of 2-propen-1-ol produced 1,2-propanediol ($m/z = 57$).

Generally, organic pollutants on mineralization or degradation get converted into carbon dioxide, water, and some inorganic ions. However, nitrogen-containing aliphatic organic pollutants decompose into fragments like amides and carboxylic acids, which further degrade to CO_2 , H_2O , and inorganic ions. As is known, this mineralization ability of the material plays a vital role in scrutinizing the catalytic potential of a photocatalyst. Here, the mineralization of antibiotic gemifloxacin (GMF) was examined over the ternary hybrid PZFW15 at a periodic interval via total organic carbon (TOC) analysis. Further, the extent of degradation or mineralization in terms of TOC was calculated using the following equation (eq 5).

$$\% \text{ of mineralization} = \frac{T_0 - T_t}{T_0} \quad (5)$$

Here, T_0 and T_t stand for TOC of the model pollutant, i.e., GMF before and after photon irradiation, respectively. Figure S15 depicts the percentage of mineralization at different time gaps. It was found that in the present investigation the mineralization percentage is around 69% at the end of 120 min. This indicates that GMF has been mineralized to CO_2 , H_2O , and other fragmented/intermediate compounds, which are well detected and confirmed by the LCMS study.

Additionally, the modified version of Z-scheme catalytic systems was regarded as the most effective photocatalyst for photoredox reaction owing to the availability of highly reducing electrons and highly oxidizing holes for both oxidation and reduction processes. In particular, this type of S-scheme system shows promising H_2 evolution activity. In this work, photocatalytic hydrogen generations of the synthesized samples (PPY, ZnF, WO_{3-x} , ZFW15, and PZFW15) were investigated under visible-light illumination under ambient conditions. First, we optimized the experimental conditions involving catalyst concentrations (5, 10, 15, 20, and 25 mg) and the sacrificial reagent (TEOA, isopropanol, ethanol, and methanol) over the best catalyst that we screened from the GMF degradation test, i.e., PZFW15 (Figure S16). From the above optimization experiment, we conclude that the 15 mg sample dose and methanol as the sacrificial agent show the best hydrogen evolution reaction. Hence, by suspending 15 mg of catalysts in a methanol/water (v/v: 1:9) solution, the water reduction experiment was carried out. Importantly, no H_2 gas was detected in the absence of light and the catalyst, which proves the pivotal role of the catalyst and light for the water-splitting reaction, as shown in Figure 8d. Because of the positive CB potential, WO_{3-x} does not show any H_2 production, while ZnF exhibits a low hydrogen activity of $296 \mu\text{mol h}^{-1}$ due to particle agglomeration and rapid recombination of photoproducted charge carriers. However, the binary hybrid of ZnF and WO_{3-x} (ZFW15 hybrid) depicts a hydrogen evolution rate of $449 \mu\text{mol h}^{-1}$, which was 1.51 times that of the pure ZnF. This escalation in the photoactivity could be ascribed to the formulation of the OV-mediated S-scheme, which improves the charge separation efficiency and thereby increases the lifetime of electron–hole pairs. In the proposed S-scheme mechanism, the photoproducted electrons of WO_{3-x} get trapped in its OV energy level, which further combines with holes available at ZnF VB, promoting spatial charge separation. The coexistence of W^{5+} and W^{6+} states was confirmed from the XPS analysis, and the intervalence charge transfer between the W^{5+} and W^{6+} ions along with OVs was also responsible for the enhancement in photoactivity.^{22,44,45} Further elevation in the rate of hydrogen generation was perceived after the introduction of PPY to the ZFW15 junction specimen. The electron accumulated in the LUMO of ZnF was injected into the PPY to trigger the H_2 evolution reaction. Specifically, the PZFW15 ternary heterostructure exhibits a maximum of $657 \mu\text{mol}$ of H_2 production, which is 2.2-fold higher than that of the solitary ZnF. The solitary PPY also displays a hydrogen activity of $80 \mu\text{mol h}^{-1}$. Moreover, the energy conversion efficiency of the best photocatalyst, i.e., the 2BG/ZnF@20PPY ternary system, was found to be 4.92%. The lowest PL intensity, EIS, highest absorbance, photocurrent density, and the lifetime of PZFW15 corroborate with the photocatalytic activity. Further, the advanced photocatalytic

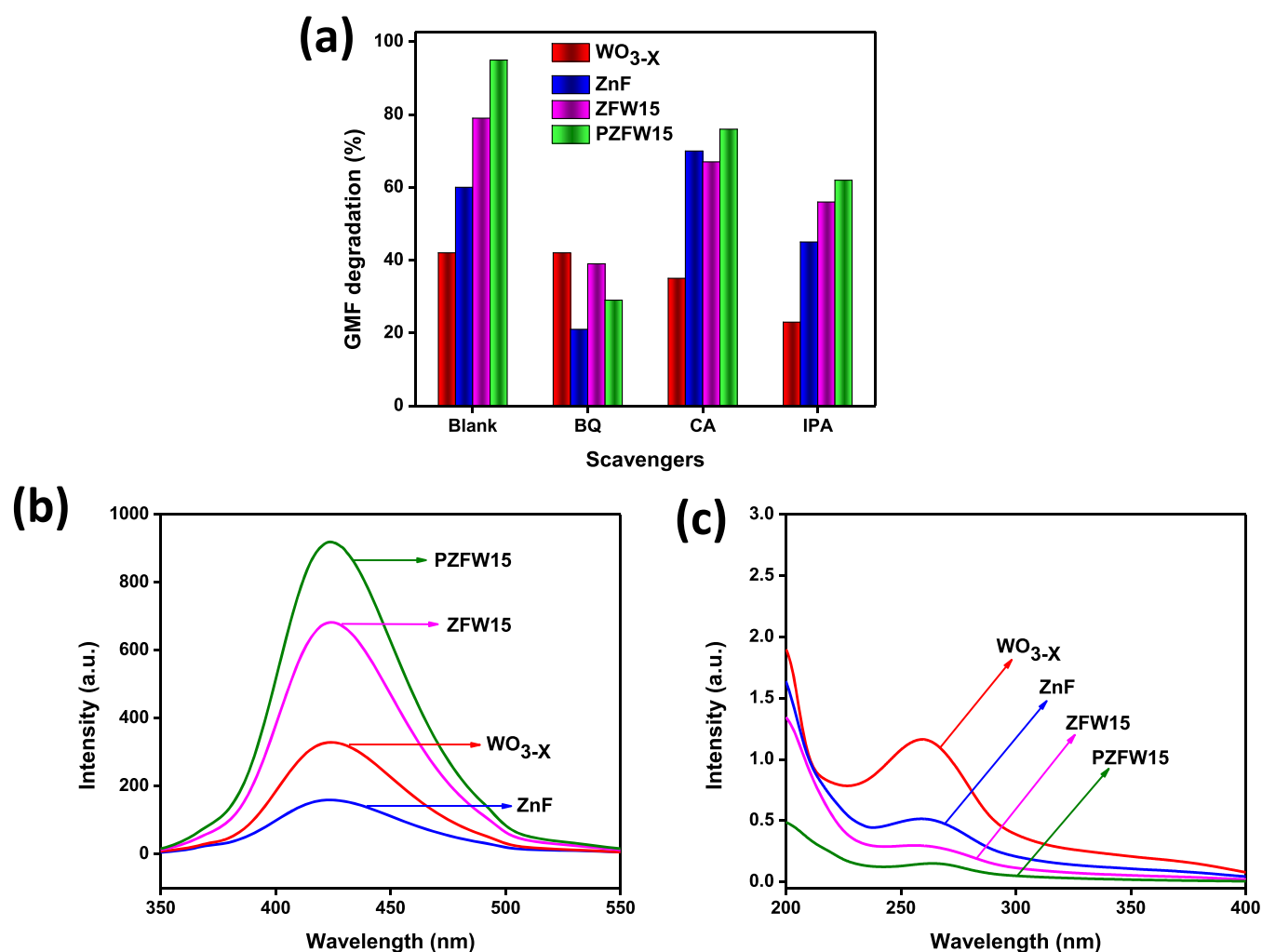


Figure 10. (a) Scavenger test, (b) TA test, and (c) NBT experiments by ZnF, WO_{3-x}, ZFW15, and PZFW15 samples.

activity of our designed S-scheme photocatalyst has been compared with other S-scheme systems (displayed in Table S4).

The excellent photocatalytic activities exerted by the ternary heterojunction over H₂ evolution and GMF degradation compared to other synthesized specimens led to an interest in knowing about the importance of photoinduced charge carriers in photoactivity. For the sake of clarifying the photocatalytic mechanisms of GMF degradation, the generations and involvement of major active species are further investigated by tracing experiments. In this free radical experiment, ZnF, WO_{3-x}, ZFW15, and PZFW15 were studied for GMF degradation, as shown in Figure 10a. Citric acid (CA), *p*-benzoquinone (*p*-BQ), and isopropyl alcohol (IPA) were employed as quenchers for trapping the h⁺, •O₂⁻, and •OH species, respectively, and to investigate their influence on the photodegradation process. From the figure, it can be observed that in the absence of any scavenging agent, the degradation ratio of GMF reached 32, 60, 79, and 95% for WO_{3-x}, ZnF, ZFW15, and PZFW15, respectively. However, the degradation of GMF was restricted to a minimum in the presence of benzoquinone, while IPA has a minimal inhibitory effect. The holes have no impact on the degradation process; rather, quenching of holes results in improving the degradation efficiency, which explains that holes are not the active species in solitary ZnF and the increase in activity is because of the

enhanced separation of photogenerated charge carriers. The quenching of holes leads to more electrons taking part in the reduction of O₂ to •O₂⁻ radicals. Therefore, oxides are the principal species responsible for degradation in solitary ZnF, and the •OH radical plays a minor role in the degradation activity. Similarly, for the WO_{3-x} component, the degradation efficiency was restricted in the presence of IPA, which suggests that •OH is the active species involved in the degradation process. However, the holes show marginal restriction of the photodegradation activity, while •O₂⁻ has no hand in the photocatalytic activity of GMF. Moreover, the photoactivity of the ZFW15 system was drastically reduced after the addition of IPA and *p*-BQ, which decrease almost 10 times and 8 times, respectively, compared to controlled studies. This outcome suggests that •OH and •O₂⁻ radicals are the chief active species that had the most pronounced influence on the GMF degradation process. The quenching test for •OH and •O₂⁻ radicals further confirms the formation of the S-scheme via OV_s between WO_{3-x} and ZnF. This is because the CB of WO_{3-x} does not have the required potential to generate H₂ and also reduces O₂ to the •O₂⁻ radical; likewise, the VB of ZnF cannot oxidize H₂O to the hydroxyl radical, which occurs if the double charge-transfer mechanism is taken into consideration. Rather, the S-scheme-type charge migration process occurs, which strongly explains the charge-transfer and reaction mechanistic route (details described in the successive

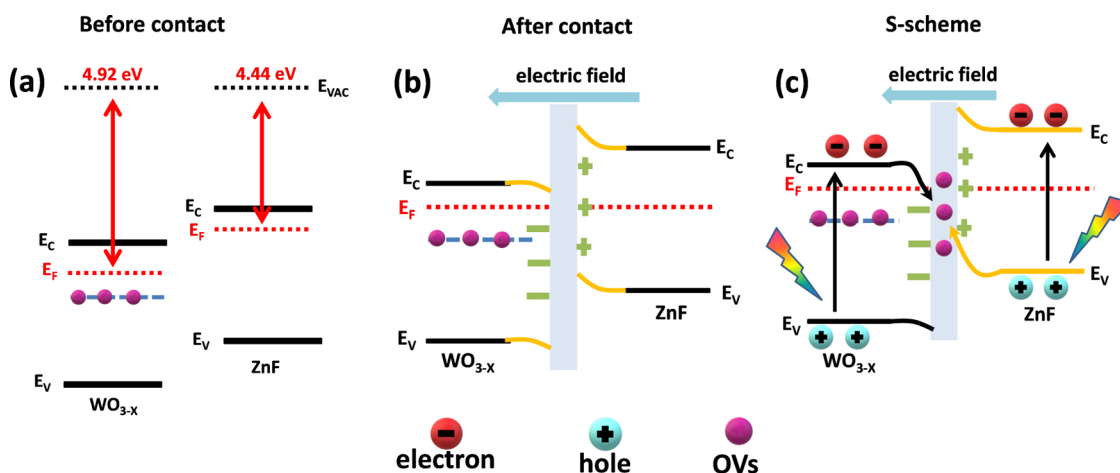


Figure 11. (a) Work functions of ZnF and WO_{3-x} before contact. (b) Internal electric field and band-edge bending at the interface of the ZFW15 after contact. (c) S-scheme charge-transfer mechanism between ZnF and WO_{3-x} under light irradiation.

section). Similar results were also obtained for the PZFW15 ternary system.

To verify the above postulation, terephthalic acid (TA) was utilized as a probe molecule to corroborate the generation of $\cdot\text{OH}$ radicals by luminescence analysis.⁴⁸ Figure 10b displays that the PL intensity at 423 nm gradually increases as we move from solitary ZnF to the ternary system. The $\cdot\text{OH}$ cannot be generated on the VB of ZnF as the minimum potential requirement was -6.49 eV vs the vacuum (1.99 eV vs NHE). However, a weak spectrum was observed for ZnF, which explains the indirect formation of $\cdot\text{OH}$ radicals. Moreover, in comparison to WO_{3-x} , the higher PL spectrum of ZFW15 suggests the formation of more numbers of $\cdot\text{OH}$ radicals. The ternary hybrid exhibits the highest PL intensity, suggesting that $\cdot\text{OH}$ was promoted on the ternary heterojunction directly and indirectly. Similarly, the formation of $\cdot\text{O}_2^-$ was confirmed by UV-vis spectroscopy taking NBT as the probe agent.⁴⁸ Because of the lower CB potential, i.e., -4.75 eV vs vacuum ($+0.25$ eV vs NHE), the WO_{3-x} was unable to generate $\cdot\text{O}_2^-$ radicals, as shown in Figure 10c. Besides, a gradual decrease in NBT spectra was noticed from ZnF to ZFW15, and PZFW15 confirms the formation of more amount of $\cdot\text{O}_2^-$ radicals. After the fabrication of a binary or ternary heterostructure with band aligning, the electrons move from the higher CB of ZnF to the lower CB of WO_{3-x} ; similarly, the corresponding holes transferred from the more positive VB potential of WO_{3-x} to the less positive VB potential of ZnF, resulting in more accumulation of electrons on the CB of WO_{3-x} and holes on the VB of ZnF. However, the electrons and holes could not react with O_2 and OH^- to generate $\cdot\text{O}_2^-$ and $\cdot\text{OH}$, respectively. Therefore, the maximum proportion of electrons is supposed to reside at the CB of ZnF in binary and ternary heterostructures to produce more effective $\cdot\text{O}_2^-$ radicals. Henceforth, the above discussion indicates that the charge separation in ZFW15 and PZFW15 undergoes an OV-mediated S-scheme rather than a traditional double charge separation. Furthermore, the formation of $\cdot\text{O}_2^-$ and $\cdot\text{OH}$ was confirmed from the DMPO-trapping electron spin resonance (ESR) characterization under visible-light illumination. As illustrated in Figure S17, the featured DMPO- O_2^- adducts ESR signals of ZnF and ZFW15, which suggests the formation of $\cdot\text{O}_2^-$ radicals in both samples. However, these signals of $\cdot\text{O}_2^-$ were hardly detected for the WO_{3-x} specimen as the CB does

not meet the required potential for the generation of $\cdot\text{O}_2^-$. Similarly, weak characteristic peaks for $\cdot\text{OH}$ radicals were observed for the ZnF component, whereas obvious characteristic foursome signals were observed for both WO_{3-x} and ZFW15 systems, indicating that $\cdot\text{OH}$ radicals are produced and involved in the degradation process. In comparison to solitary ZnF and WO_{3-x} components, more $\cdot\text{O}_2^-$ and $\cdot\text{OH}$ were generated in the ZFW15 system. Henceforth, the quenching and ESR experiments establish that $\cdot\text{OH}$ and $\cdot\text{O}_2^-$ are key species involved in the photodegradation of GMF and further confirm that the charge migration pathway does not obey the traditional type-II process but rather follows an S-scheme tactic, which is in good agreement with the quenching results.

The practical implication of the fabricated ternary system entirely depends on its photodurability and reusability capability. As shown in Figure S18a,b, the designed ternary system displays consistency toward antibiotic detoxification and H_2 evolution up to three successive cycles. However, the detoxification efficiency and H_2 generation rate suffered a minimal decline in the 4th cycle, attributed to the wear and tear of the catalyst surface and inevitable catalyst loss during the intermittent recovery process. Further, XRD and TEM images of the ternary heterostructure after sequential reuses demonstrated a well-conserved crystal structure with a nominal decline in the peak intensity compared to the idle one (Figure S18c,d). This further validates the superior photostability of the PZFW15 heterostructure.

To date, it has been well understood that charge transfer in the ternary system occurs at a faster rate in comparison to binary and single systems. However, effective separation along with the shipment of photoproduced electrons and holes is considered as the two standing pillars upon which photocatalytic efficiency settles on. To establish the best possible charge-transfer pathways, we have considered the S-scheme charge-transfer mechanism. Thus, the charge-transfer dynamics and band-edge positions both should be considered in deciding the e-h transfer pathway for reduction and oxidation reactions.

On account of the unification of both semiconducting materials, the band-gap energy and band-edge positions have the utmost dynamics to explain the charge-transfer dynamics. As explained above, by the combination of UPS, VB-XPS, and

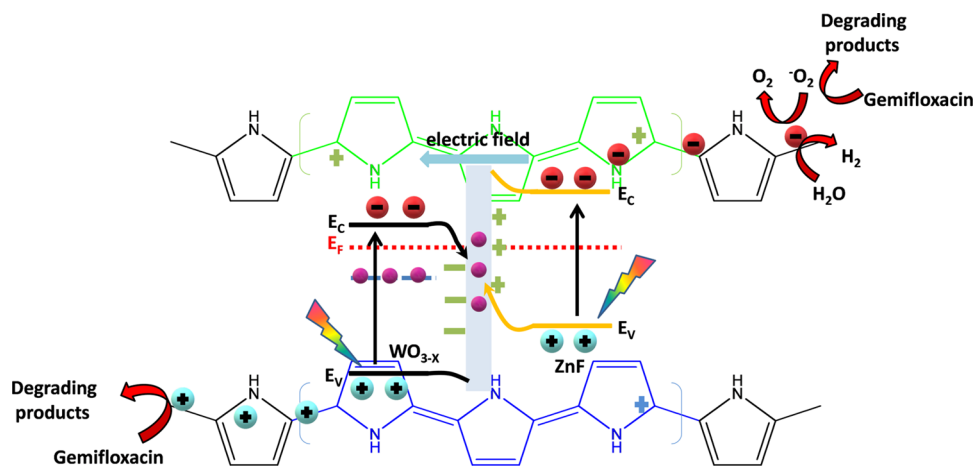


Figure 12. Schematic diagram of photocatalytic degradation of GMF and H₂ generation over PZFW15.

optical band-gap measurement results, the work functions of ZnF and WO_{3-x} were estimated to be 4.44 and 4.92 eV, respectively. The above results and discussions permit an imaginable interface formation, i.e., the S-scheme heterojunction for the electron-transfer pathway between ZnF and WO_{3-x}, as shown in Figure 11. However, it was found that ZnF was a reduction photocatalyst with a smaller work function (4.44 eV), whereas WO_{3-x} was an oxidation photocatalyst with a higher work function (4.92 eV) (Figure 11a). As the work function of ZnF was lower than that of WO_{3-x}, when both come in close contact, the electrons in ZnF spontaneously rush to WO_{3-x} across their interface to attain the Fermi energy-level equilibration (Figure 11b). As a result, ZnF becomes positively charged on losing electrons, while WO_{3-x} becomes negatively charged at the interface on receiving the electrons. This type of electron transition leads to the formation of an internal built-in electric field at the interfacial region of ZnF and WO_{3-x} (forming the space-charge region).⁶ In the meantime, the band edge of ZnF bends upward with the shipment of the electron, whereas the band edge of WO_{3-x} bends downward owing to the accumulation of electrons, as illustrated in Figure 11b. Under visible-light illumination, the electrons were excited from the valence band (VB) to the conduction band (CB) of the respective combining species, i.e., ZnF and WO_{3-x}. However, in the case of WO_{3-x}, the excited electrons migrate directly from the VB to the energy band of OVs as well as some electrons in the CB of WO_{3-x} further get trapped in the OV sub-band. As the OV energy levels of WO_{3-x} are near the VB of ZnF, the electrons in the OV level of WO_{3-x} combine with the photogenerated holes in the VB of ZnF quite easily, making the highly reducing photoelectrons in the CB of ZnF and the highly oxidizing photoinduced holes in the VB of WO_{3-x} freely available to carry out the catalytic reaction (Figure 11c). Further, W⁵⁺ ions produced because of OVs get oxidized to W⁶⁺ by the holes of ZnF, and simultaneously, the W⁶⁺ ions so produced on WO_{3-x} are reduced to W⁵⁺ ions by the OV electrons back at the interface region, and all of this happens only under photon irradiation. In this way, OVs act as electron mediators to establish a charge-carrier migration bridge between the VB of ZnF and the CB of WO_{3-x}, which accelerates the shipment and separation of photoproducted carriers at the S-scheme junction interface.^{16,49,50} The internal electric field, induced band-bending energy, Coulombic interaction, and OVs accelerate the union of the electron

(CB of WO_{3-x}) and hole (VB of ZnF) via the S-scheme pathway.^{6,14,16,49,50} This proposed S-scheme pathway has now achieved the required potential for the water reduction reaction and superoxide and hydroxyl radical generation.

The binary catalytic system was further modified with PPY, where PPY behaves as e⁻-h⁺ shrinkers producing the ternary heterostructure, i.e., PZFW15. Moreover, the separation of e⁻-h⁺ pairs was enhanced by the polaron and bipolaron species of PPY generated via the oxidative π -bond cleavage. As a result, electrons in the CB of ZnF migrate rapidly to positive polaron species, which reduces H₂O, ensuring the higher production of H₂ gas, and also reduces the dissolved O₂ to [•]O₂⁻ radicals, which are primarily responsible for GMF degradation (concluded by the scavenger experiment). On the other hand, the holes in the VB of WO_{3-x} were further trapped by bipolaron species and then react with H₂O to form the [•]OH radical, which later degrades GMF into oxidizing products (Figure 12). Hence, it can be concluded that the PZFW15 ternary heterostructure establishes a polaron- and bipolaron-induced S-scheme type of charge migration pathway, which not only fastens the shipment and isolation of photoproducted excitons but also maintains a stronger redox ability toward the degradation of antibiotic-GMF and the H₂ generation reaction.

CONCLUSIONS

In summary, a multistep synthesis procedure of a PPY-supported innovative S-scheme heterostructure photocatalyst built from OV-induced WO_{3-x} and ZnF was developed. In comparison to parent and binary materials, the ternary PZFW15 exhibits the highest catalytic activity toward 100 ppm of GMF degradation (95%, 60 min) and H₂ evolution (657 μ mol h⁻¹). The presence of PPY having a polaron and bipolaron species plays a key role as electron and hole acceptor from the S-scheme-based ZFW15 nano hybrid, respectively, which promotes exciton separation and ultimately boosts the GMF degradation and H₂ generation. The combined effect of the OV-mediated S-scheme junction and radical cations of PPY increases the lifetime of photoinduced charge carriers, which leads to enhanced photoreduction and oxidation activity over the ternary PZFW15 catalyst. The XPS and experimentally found work function confirm the formation of the S-scheme junction and its correctness in between ZnF and WO_{3-x}. The outcome of this research opens a new

opportunity for rationally fabricating highly effective S-scheme systems supported on conducting polymers exhibiting polaron and bipolaron properties.

■ ASSOCIATED CONTENT

Supporting Information

The Supporting Information is available free of charge at <https://pubs.acs.org/doi/10.1021/acsomega.1c03705>.

Experimental procedures, figures, tables, detailed information about the effect of various parameters (dose, concentration, anions, and cations on the photo-degradation of GMF with PZFW15 along with stability test), ESR analysis, H₂ evolution under different parameters (PDF)

■ AUTHOR INFORMATION

Corresponding Author

Kulamani Parida – Centre for Nanoscience and Nanotechnology, SOA (Deemed to be University), Bhubaneswar 751030 Odisha, India; orcid.org/0000-0001-7807-5561; Phone: +91-674-2379425; Email: paridakulamani@yahoo.com, kulamaniparida@soa.ac.in; Fax: +91-674-2581637

Authors

Kundan Kumar Das – Centre for Nanoscience and Nanotechnology, SOA (Deemed to be University), Bhubaneswar 751030 Odisha, India

Dipti Prava Sahoo – Centre for Nanoscience and Nanotechnology, SOA (Deemed to be University), Bhubaneswar 751030 Odisha, India

Sriram Mansingh – Centre for Nanoscience and Nanotechnology, SOA (Deemed to be University), Bhubaneswar 751030 Odisha, India; orcid.org/0000-0002-7679-3663

Complete contact information is available at: <https://pubs.acs.org/doi/10.1021/acsomega.1c03705>

Notes

The authors declare no competing financial interest.

■ ACKNOWLEDGMENTS

The authors are greatly obliged to the SOA (Deemed to be University) management for their encouragement and support in publishing the work.

■ REFERENCES

- (1) Li, C.; Xu, Y.; Tu, W.; Chen, G.; Xu, R. Metal-free photocatalysts for various applications in energy conversion and environmental purification. *Green Chem.* **2017**, *19*, 882–899.
- (2) Liu, X.; Iocozzia, J.; Wang, Y.; Cui, X.; Chen, Y.; Zhao, S.; Li, Z.; Lin, Z. Noble metal–metal oxide nanohybrids with tailored nanostructures for efficient solar energy conversion, photocatalysis and environmental remediation. *Energy Environ. Sci.* **2017**, *10*, 402–434.
- (3) Mansingh, S.; Sultana, S.; Acharya, R.; Ghosh, M. K.; Parida, K. M. Efficient Photon Conversion via Double Charge Dynamics CeO₂–BiFeO₃ p–n Heterojunction Photocatalyst Promising toward N₂ Fixation and Phenol–Cr (VI) Detoxification. *Inorg. Chem.* **2020**, *59*, 3856–3873.
- (4) Dai, B.; Fang, J.; Yu, Y.; Sun, M.; Huang, H.; Lu, C.; Kou, J.; Zhao, Y.; Xu, Z. Construction of Infrared Light Responsive

Photoinduced Carriers Driver for Enhanced Photocatalytic Hydrogen Evolution. *Adv. Mater.* **2020**, *32*, No. 1906361.

- (5) Zhao, F.; Yin, D.; Khaing, K. K.; Liu, B.; Chen, T.; Deng, L.; Li, L.; Guo, X.; Wang, J.; Xiao, S.; Ouyang, Y. Fabrication of hierarchical Co₉S₈@ ZnAgInS heterostructured cages for highly efficient photocatalytic hydrogen generation and pollutants degradation. *Inorg. Chem.* **2020**, *59*, 7027–7038.

- (6) Fu, J.; Xu, Q.; Low, J.; Jiang, C.; Yu, J. Ultrathin 2D/2D WO₃/g-C₃N₄ step-scheme H₂-production photocatalyst. *Appl. Catal., B* **2019**, *243*, 556–565.

- (7) Das, K. K.; Patnaik, S.; Nanda, B.; Pradhan, A. C.; Parida, K. ZnFe₂O₄-Decorated Mesoporous Al₂O₃ Modified MCM-41: A Solar-Light-Active Photocatalyst for the Effective Removal of Phenol and Cr (VI) from Water. *ChemistrySelect* **2019**, *4*, 1806–1819.

- (8) Huang, Y.; Zhu, D.; Zhang, Q.; Zhang, Y.; Cao, J. J.; Shen, Z.; Ho, W.; Lee, S. C. Synthesis of a Bi₂O₂CO₃/ZnFe₂O₄ heterojunction with enhanced photocatalytic activity for visible light irradiation-induced NO removal. *Appl. Catal., B* **2018**, *234*, 70–78.

- (9) Han, J.; Lan, Y.; Song, Q.; Yan, H.; Kang, J.; Guo, Y.; Liu, Z. Zinc ferrite-based p–n homojunction with multi-effect for efficient photoelectrochemical water splitting. *Chem. Commun.* **2020**, *56*, 13205–13208.

- (10) Tan, P.; Liu, Y.; Zhu, A.; Zeng, W.; Cui, H.; Pan, J. Rational design of Z-scheme system based on 3D hierarchical CdS supported 0D Co₉S₈ nanoparticles for superior photocatalytic H₂ generation. *ACS Sustainable Chem. Eng.* **2018**, *6*, 10385–10394.

- (11) Dai, Z.; Zhen, Y.; Sun, Y.; Li, L.; Ding, D. ZnFe₂O₄/g-C₃N₄ S-scheme photocatalyst with enhanced adsorption and photocatalytic activity for uranium (VI) removal. *Chem. Eng. J.* **2021**, *415*, No. 129002.

- (12) Rawal, S. B.; Kang, H. J.; Won, D. I.; Lee, W. I. Novel ZnFe₂O₄/WO₃, a highly efficient visible-light photocatalytic system operated by a Z-scheme mechanism. *Appl. Catal., B* **2019**, *256*, No. 117856.

- (13) Rong, X.; Chen, H.; Rong, J.; Zhang, X.; Wei, J.; Liu, S.; Zhou, X.; Xu, J.; Qiu, F.; Wu, Z. An all-solid-state Z-scheme TiO₂/ZnFe₂O₄ photocatalytic system for the N₂ photofixation enhancement. *Chem. Eng. J.* **2019**, *371*, 286–293.

- (14) Wang, J.; Zhang, Q.; Deng, F.; Luo, X.; Dionysiou, D. D. Rapid toxicity elimination of organic pollutants by the photocatalysis of environment-friendly and magnetically recoverable step-scheme SnFe₂O₄/ZnFe₂O₄ nano-heterojunctions. *Chem. Eng. J.* **2020**, *379*, No. 122264.

- (15) Meng, A.; Cheng, B.; Tan, H.; Fan, J.; Su, C.; Yu, J. TiO₂/polydopamine S-scheme heterojunction photocatalyst with enhanced CO₂-reduction selectivity. *Appl. Catal., B* **2021**, *289*, No. 120039.

- (16) Du, X.; Song, S.; Wang, Y.; Jin, W.; Ding, T.; Tian, Y.; Li, X. Facile one-pot synthesis of defect-engineered step-scheme WO₃/g-C₃N₄ heterojunctions for efficient photocatalytic hydrogen production. *Catal. Sci. Technol.* **2021**, *11*, 2734.

- (17) Xing, X.; Zhu, H.; Zhang, M.; Hou, L.; Li, Q.; Yang, J. Interfacial oxygen vacancy layer of a Z-scheme BCN–TiO₂ heterostructure accelerating charge carrier transfer for visible light photocatalytic H₂ evolution. *Catal. Sci. Technol.* **2018**, *8*, 3629–3637.

- (18) Wu, S.; Yu, X.; Zhang, J.; Zhang, Y.; Zhu, Y.; Zhu, M. Construction of BiOCl/CuBi₂O₄ S-scheme heterojunction with oxygen vacancy for enhanced photocatalytic diclofenac degradation and nitric oxide removal. *Chem. Eng. J.* **2021**, *411*, No. 128555.

- (19) Zhou, Z.; Niu, X.; Zhang, Y.; Wang, J. Janus MoSSe/WSeTe heterostructures: a direct Z-scheme photocatalyst for hydrogen evolution. *J. Mater. Chem. A* **2019**, *7*, 21835–21842.

- (20) Dou, L.; Jin, X.; Chen, J.; Zhong, J.; Li, J.; Zeng, Y.; Duan, R. One-pot solvothermal fabrication of S-scheme OVs-Bi₂O₃/Bi₂SiO₅ microsphere heterojunctions with enhanced photocatalytic performance toward decontamination of organic pollutants. *Appl. Surf. Sci.* **2020**, *527*, No. 146775.

- (21) Sahoo, D. P.; Patnaik, S.; Parida, K. Construction of a Z-scheme dictated WO₃–X/Ag/ZnCr LDH synergistically visible light-induced

photocatalyst towards tetracycline degradation and H₂ evolution. *ACS Omega* **2019**, *4*, 14721–14741.

(22) Huang, S.; Long, Y.; Ruan, S.; Zeng, Y. J. Enhanced Photocatalytic CO₂ Reduction in Defect-Engineered Z-Scheme WO_{3-x}/g-C₃N₄ Heterostructures. *ACS Omega* **2019**, *4*, 15593–15599.

(23) Xiao, Y.; Tao, X.; Qiu, G.; Dai, Z.; Gao, P.; Li, B. Optimal synthesis of a direct Z-scheme photocatalyst with ultrathin W₁₈O₄₉ nanowires on g-C₃N₄ nanosheets for solar-driven oxidation reactions. *J. Colloid Interface Sci.* **2019**, *550*, 99–109.

(24) Xiao, Y.; He, Z.; Wang, R.; Tao, X.; Li, B. Synthesis of WO₃ nanofibers decorated with BiOCl nanosheets for photocatalytic degradation of organic pollutants under visible light. *Colloids Surf., A* **2019**, *580*, No. 123752.

(25) Wang, R.; Qiu, G.; Xiao, Y.; Tao, X.; Peng, W.; Li, B. 2019. Optimal construction of WO₃·H₂O/Pd/CdS ternary Z-scheme photocatalyst with remarkably enhanced performance for oxidative coupling of benzylamines. *J. Catal.* **2019**, *374*, 378–390.

(26) Das, K. K.; Patnaik, S.; Mansingh, S.; Behera, A.; Mohanty, A.; Acharya, C.; Parida, K. M. Enhanced photocatalytic activities of polypyrrole sensitized zinc ferrite/graphitic carbon nitride n-n heterojunction towards ciprofloxacin degradation, hydrogen evolution and antibacterial studies. *J. Colloid Interface Sci.* **2020**, *561*, 551–567.

(27) Kumar, T. R. N.; Karthik, P.; Neppolian, B. Polaron and bipolaron induced charge carrier transportation for enhanced photocatalytic H₂ production. *Nanoscale* **2020**, *12*, 14213–14221.

(28) Wang, Y.; Cai, J.; Wu, M.; Chen, J.; Zhao, W.; Tian, Y.; Ding, T.; Zhang, J.; Jiang, Z.; Li, X. Rational construction of oxygen vacancies onto tungsten trioxide to improve visible light photocatalytic water oxidation reaction. *Appl. Catal., B* **2018**, *239*, 398–407.

(29) Boruah, P. J.; Khanikar, R. R.; Bailung, H. Synthesis and characterization of oxygen vacancy induced narrow bandgap tungsten oxide (WO_{3-x}) nanoparticles by plasma discharge in liquid and its photocatalytic activity. *Plasma Chem. Plasma Process.* **2020**, *40*, 1019–1036.

(30) Lv, C.; Yan, C.; Chen, G.; Ding, Y.; Sun, J.; Zhou, Y.; Yu, G. An Amorphous Noble-Metal-Free Electrocatalyst that Enables Nitrogen Fixation under Ambient Conditions. *Angew. Chem.* **2018**, *130*, 6181–6184.

(31) Patnaik, S.; Das, K. K.; Mohanty, A.; Parida, K. Enhanced photo catalytic reduction of Cr (VI) over polymer-sensitized g-C₃N₄/ZnFe₂O₄ and its synergism with phenol oxidation under visible light irradiation. *Catal. Today* **2018**, *315*, 52–66.

(32) Singh, J. P.; Srivastava, R. C.; Agrawal, H. M.; Kumar, R. Micro-Raman investigation of nanosized zinc ferrite: effect of crystallite size and fluence of irradiation. *J. Raman Spectrosc.* **2011**, *42*, 1510–1517.

(33) Iftikhar, M.; Ali, B.; Nisar, T.; Wagner, V.; Haider, A.; Hussain, S.; Bahadar, A.; Saleem, M.; Abbas, S. M. Improving Lithium-Ion Half-/Full-Cell Performance of WO₃-Protected SnO₂ Core-Shell Nanoarchitectures. *ChemSusChem* **2021**, *14*, 917–928.

(34) Shao, C.; Malik, A. S.; Han, J.; Li, D.; Dupuis, M.; Zong, X.; Li, C. Oxygen vacancy engineering with flame heating approach towards enhanced photoelectrochemical water oxidation on WO₃ photoanode. *Nano Energy* **2020**, *77*, No. 105190.

(35) Han, C.; Shi, R.; Zhou, D.; Li, H.; Xu, L.; Zhang, T.; Li, J.; Kang, F.; Wang, G.; Li, B. High-energy and high-power nonaqueous lithium-ion capacitors based on polypyrrole/carbon nanotube composites as pseudocapacitive cathodes. *ACS Appl. Mater. Interfaces* **2019**, *11*, 15646–15655.

(36) Pruna, A.; Shao, Q.; Kamruzzaman, M.; Li, Y. Y.; Zapien, J. A.; Pullini, D.; Mataix, D. B.; Ruotolo, A. Effect of ZnO core electrodeposition conditions on electrochemical and photocatalytic properties of polypyrrole-graphene oxide shelled nanoarrays. *Appl. Surf. Sci.* **2017**, *392*, 801–809.

(37) Beji, Z.; Sun, M.; Smiri, L. S.; Herbst, F.; Mangeney, C.; Ammar, S. Polyol synthesis of non-stoichiometric Mn–Zn ferrite nanocrystals: structural/microstructural characterization and catalytic application. *RSC Adv.* **2015**, *5*, 65010–65022.

(38) Zhou, J.; An, X.; Tang, Q.; Lan, H.; Chen, Q.; Liu, H.; Qu, J. Dual channel construction of WO₃ photocatalysts by solution plasma for the persulfate-enhanced photodegradation of bisphenol A. *Appl. Catal., B* **2020**, *277*, No. 119221.

(39) Yan, J.; Wang, T.; Wu, G.; Dai, W.; Guan, N.; Li, L.; Gong, J. Tungsten oxide single crystal nanosheets for enhanced multichannel solar light harvesting. *Adv. Mater.* **2015**, *27*, 1580–1586.

(40) Sultana, S.; Mansingh, S.; Parida, K.M. Rational design of light induced self healed Fe based oxygen vacancy rich CeO₂ (CeO₂ NS–FeOOH/Fe₂O₃) nanostructure materials for photocatalytic water oxidation and Cr (VI) reduction. *J. Mater. Chem. A* **2018**, *6*, 11377–11389.

(41) Xia, P.; Cao, S.; Zhu, B.; Liu, M.; Shi, M.; Yu, J.; Zhang, Y. Designing a 0D/2D S-scheme heterojunction over polymeric carbon nitride for visible-light photocatalytic inactivation of bacteria. *Angew. Chem., Int. Ed.* **2020**, *59*, 5218–5225.

(42) Liu, H.; Tian, K.; Ning, J.; Zhong, Y.; Zhang, Z.; Hu, Y. One-step solvothermal formation of Pt nanoparticles decorated Pt²⁺-doped α-Fe₂O₃ nanoplates with enhanced photocatalytic O₂ evolution. *ACS Catal.* **2019**, *9*, 1211–1219.

(43) Yang, L.; Lv, M.; Song, Y.; Yin, K.; Wang, X.; Cheng, X.; Cao, K.; Li, S.; Wang, C.; Yao, Y.; Luo, W. Porous Sn₃O₄ nanosheets on PPy hollow rod with photo-induced electrons-oriented migration for enhanced visible-light hydrogen production. *Appl. Catal., B* **2020**, *279*, No. 119341.

(44) Yang, B.; Zheng, J.; Li, W.; Wang, R.; Li, D.; Guo, X.; Rodriguez, R. D.; Jia, X. Engineering Z-scheme TiO₂-OV-BiOCl via oxygen vacancy for enhanced photocatalytic degradation of imidacloprid. *Dalton Trans.* **2020**, *49*, 11010–11018.

(45) Jeong, I.; Jo, C.; Anthonysamy, A.; Kim, J. M.; Kang, E.; Hwang, J.; Ramasamy, E.; Rhee, S. W.; Kim, J. K.; Ha, K. S.; Jun, K. W. Ordered Mesoporous Tungsten Suboxide Counter Electrode for Highly Efficient Iodine-Free Electrolyte-Based Dye-Sensitized Solar Cells. *ChemSusChem* **2013**, *6*, 299–307.

(46) Gholami, P.; Khataee, A.; Soltani, R.D.C.; Dinpazhoh, L.; Bhatnagar, A. Photocatalytic degradation of gemifloxacin antibiotic using Zn-Co-LDH@ biochar nanocomposite. *J. Hazard. Mater.* **2020**, *382*, No. 121070.

(47) Gholami, P.; Dinpazhoh, L.; Khataee, A.; Orooji, Y. Sonocatalytic activity of biochar-supported ZnO nanorods in degradation of gemifloxacin: synergy study, effect of parameters and phytotoxicity evaluation. *Ultrason. Sonochem.* **2019**, *55*, 44–56.

(48) Sahoo, D. P.; Das, K. K.; Patnaik, S.; Parida, K. Double charge carrier mechanism through 2D/2D interface-assisted ultrafast water reduction and antibiotic degradation over architectural S, P co-doped g-C₃N₄/ZnCr LDH photocatalyst. *Inorg. Chem. Front.* **2020**, *7*, 3695–3717.

(49) Ding, J.; Dai, Z.; Qin, F.; Zhao, H.; Zhao, S.; Chen, R. Z-scheme BiO_{1-x}Br/Bi₂O₂CO₃ photocatalyst with rich oxygen vacancy as electron mediator for highly efficient degradation of antibiotics. *Appl. Catal., B* **2017**, *205*, 281–291.

(50) Zhao, W.; Wang, W.; Shi, H. 2D/2D Z-scheme BiO_{1-x}Br/g-C₃N₄ heterojunction with rich oxygen vacancies as electron mediator for enhanced visible-light degradation activity. *Appl. Surf. Sci.* **2020**, *528*, No. 146925.